FULL PAPER

Dalton
www.rsc.org/dalton

Marked influence of the bridging carbonyl ligands on the photo- and electrochemistry of the clusters $[Ru_3(CO)_8(\mu\text{-}CO)_2(\alpha\text{-diimine})]$ (α-diimine = 2,2′-bipyridine, 4,4′-dimethyl-2,2′-bipyridine and 2,2′-bipyrimidine)†

Frank W. Vergeer,[a] Maria J. Calhorda,[b,c] Pavel Matousek,[d] Michael Towrie[d] and František Hartl*[a]

[a] *Institute of Molecular Chemistry, Universiteit van Amsterdam, Nieuwe Achtergracht 166, 1018 WV Amsterdam, The Netherlands. E-mail: hartl@science.uva.nl*

[b] *ITQB, Av. da República, EAN, Apart. 127, 2781-901 Oeiras, Portugal*

[c] *Departamento de Química e Bioquímica, Faculdade de Ciências, Universidade de Lisboa, 1749-016 Lisboa, Portugal*

[d] *Central Laser Facility, CCLRC Rutherford Appleton Laboratory, Chilton, Didcot, Oxfordshire, UK OX11 0QX*

Received 26th March 2003, Accepted 9th May 2003
First published as an Advance Article on the web 22nd September 2003

Bonding, photochemical and electrochemical properties of the clusters $[Ru_3(CO)_8(\mu\text{-}CO)_2(\alpha\text{-diimine})]$ (α-diimine = 2,2′-bipyridine (**1**), 4,4′-dimethyl-2,2′-bipyridine (**2**) and 2,2′-bipyrimidine (**3**)) are strongly influenced by the presence of bridging carbonyl ligands. Irradiation at 471 nm initially results in the population of a $\sigma(Ru_3)\pi^*$(α-diimine) excited state. From this state, fast decay takes place to the optically hardly directly accessible $\pi(Ru/\mu\text{-}CO)\pi^*$(α-diimine) lowest excited state. These assignments agree with theoretical (TD-DFT) results, resonance Raman and picosecond time-resolved infrared spectra. The involvement of the bridging carbonyl ligands in the electron transfer increases the energetic barrier for the formation of open-structure photoproducts such as biradicals and zwitterions. Zwitterions were therefore only obtained in strongly coordinating media such as pyridine at 250 K. The bridging carbonyl ligands also stabilize the radical anions produced upon one-electron reduction of the clusters $[Ru_3(CO)_8(\mu\text{-}CO)_2(\alpha\text{-diimine})]$ and observed with cyclic voltammetry, EPR and IR spectroelectrochemistry (for α-diimine = 2,2′-bipyrimidine). In contrast, open-triangle intermediates formed along the reduction path to $[Ru(CO)_2(\alpha\text{-diimine})]_n$ and $[Ru_2(CO)_8]^{2-}$ are more reactive than their triosmium analogues.

Introduction

The large synthetic versatility of triruthenium and triosmium carbonyl clusters has placed them among the most frequently studied compounds in the field of cluster chemistry.[1] Whereas thermal activation of these systems usually requires rather harsh conditions (elevated temperature and/or pressure) that often cause undesired side-reactions, their photo- and/or electrochemical activation may provide alternative pathways for selective product formation under mild conditions.[2–4] The rich photochemistry of the unsubstituted carbonyl clusters $[M_3(CO)_{12}]$ (M = Ru, Os) has been studied most extensively over the last decades.[4–14] Irradiation into the lowest-energy absorption bands of these clusters results in the formation of the open-structure transients $[M_3(CO)_{11}(\mu\text{-}CO)]$.[6,12,15] More recently, much attention has been devoted in our laboratory to the photochemical and redox activation of the substituted clusters $[Os_3(CO)_{10}(\alpha\text{-diimine})]$, which has led to the discovery of a variety of biradical, zwitterionic, radical anionic and dianionic open-structure intermediates, formed upon electron transfer-induced cleavage of an Os–Os(α-diimine) bond.[16–20] These intermediates are of great interest because of their potential to selectively bind and activate organic substrates. Introduction of different chelating ligands such as 1,3-dienes[21] and 4,4′,5,5′-tetramethyl-2,2′-biphosphinine[22] causes pronounced changes in the photo- and electrochemical behaviour compared to $[Os_3(CO)_{12}]$ and $[Os_3(CO)_{10}$(α-diimine)]. However, since only limited efforts have been devoted to unravel the influence of the metal core composition on the photo- and redox reactivity of these substituted carbonyl clusters, we extended our investigations to α-diimine-substituted mixed Ru/Os clusters.[23] These clusters are expected to combine the intrinsic properties of both metals in the corresponding homometallic clusters. Such an investigation of the heteronuclear clusters should essentially be preceeded by a thorough study of the bonding properties, photochemistry and redox behaviour of the α-diimine-substituted homonuclear analogues.

With this in mind, we studied the photo- and electrochemical reactivity of the clusters $[Ru_3(CO)_8(\mu\text{-}CO)_2(\alpha\text{-diimine})]$, whose structure with α-diimine = 2,2′-bipyridine (bpy) (**1**), 4,4′-dimethyl-2,2′-bipyridine (dmb) (**2**) and 2,2′-bipyrimidine (bpym) (**3**) is schematically depicted in Fig. 1. Apart from our interest in these clusters as reference compounds for the Ru/Os mixed-metal clusters, they were also found to act effectively as catalyst precursors in the electrocatalytic reduction of CO_2.[24] This behaviour is in line with the aim of our current studies to investigate the activation of small molecules and unsaturated hydrocarbons by transition metal clusters.

The most interesting feature of $[Ru_3(CO)_8(\mu\text{-}CO)_2(\alpha\text{-diimine})]$ is the presence of two bridging carbonyl ligands, with implications for the bonding properties and photo- and electrochemical reactivity of these complexes. In order to evaluate this influence, the clusters $[Os_3(CO)_{10}(\alpha\text{-diimine})]$ (α-diimine = bpy, bpym) have been chosen as proper references, for the presence of exclusively terminal CO ligands in the latter compounds and the good insight obtained into their photo- and electrochemical reactivity.[16–18,25] Finally, DFT (ADF/BP) and time-dependent DFT (TD-DFT) calculations on $[Ru_3(CO)_8(\mu\text{-}CO)_2(bpy)]$ were conducted in order to support and discuss the experimental results.

† Based on the presentation given at Dalton Discussion No. 6, 9–11 September 2003, University of York, UK.

DOI: 10.1039/b303437b

Table 1 UV–VIS absorption maxima of the clusters $[Ru_3(CO)_8(\mu\text{-}CO)_2(\alpha\text{-diimine})]$ in different solvents

Cluster	λ/nm (ε/dm^3 mol^{-1} cm^{-1})		
	Toluene	THF	Acetonitrile
$[Ru_3(CO)_8(\mu\text{-}CO)_2(bpy)]$ **1**	310 sh, 473	312 sh, 388 sh, 471 (6650)	311 sh, 388 sh, 472
$[Ru_3(CO)_8(\mu\text{-}CO)_2(dmb)]$ **2**	310 sh, 471	310 sh, 388 sh, 471 (6450)	310 sh, 385 sh, 472
$[Ru_3(CO)_8(\mu\text{-}CO)_2(bpym)]$ **3**	374 sh, 476	302 sh, 376 sh, 473 (6750)	302 sh, 376 sh, 473

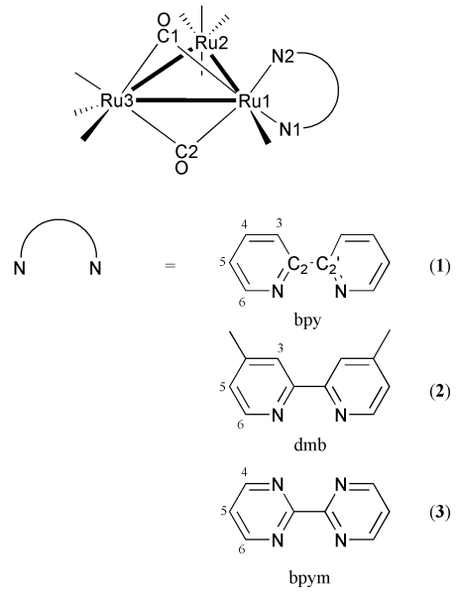

Fig. 1 Schematic structures of the clusters $[Ru_3(CO)_8(\mu\text{-}CO)_2(\alpha\text{-diimine})]$ and the α-diimine ligands used in this study.

Results

Spectroscopic properties

UV–VIS spectra. Electronic absorption spectra of the studied clusters $[Ru_3(CO)_8(\mu\text{-}CO)_2(\alpha\text{-diimine})]$ (**1**–**3**) were recorded in the 300–700 nm region. For **1** and **3**, the spectra are shown in Fig. 2. The corresponding absorption maxima are collected in Table 1. The spectra show a broad tailing band in the visible region, with a negligible solvatochromic shift in solvents of different polarity (see Table 1). Decreasing the energy of the lowest π* orbital of the α-diimine ligand on going from dmb to bpy and bpym also does not result in a shift of the lowest-energy absorption band.

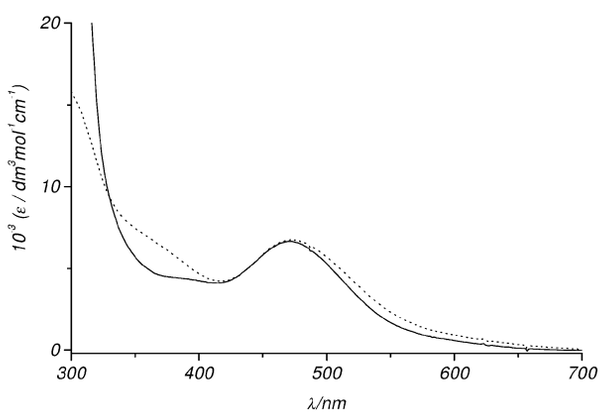

Fig. 2 UV–VIS absorption spectra of clusters **1** (—) and **3** (---) in THF at 293 K.

Resonance Raman spectra. Analysis of resonance Raman (rR) spectra facilitates assignment of electronic transitions, as the observed Raman bands belong to vibrations that are vibronically coupled to the electron transfer. The main rR bands of clusters **1** and **3** in the region 2100–200 cm^{-1} are collected in Table 2. Fig. 3 represents the rR spectrum of cluster **1** in CH_2Cl_2 obtained by excitation with 476.5 nm light.

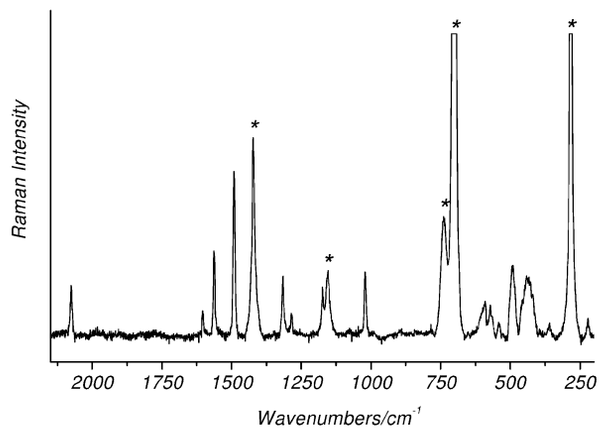

Fig. 3 Resonance Raman spectrum of cluster **1** in CH_2Cl_2 at 293 K (λ_{exc} = 476.5 nm). Asterisks (*) denote Raman bands of the solvent.

The rR spectra of both clusters show strong resonance enhancement for the α-diimine internal stretching modes between 1600 and 1000 cm^{-1} (ref. 26 and 27) and a medium rR effect for the fully symmetric ν_s(CO) mode around 2075 cm^{-1}. Importantly, several bands in the 600–220 cm^{-1} region, which belong to metal–carbon stretching and M–C–O deformation modes,[28] also show distinct rR effects. Apparently, the cluster core also participates in the lowest allowed electronic transition at 471 nm (*vide infra*).

Photochemistry

Continuous irradiation into the lowest-energy absorption band of $[Ru_3(CO)_8(\mu\text{-}CO)_2(\alpha\text{-diimine})]$ at room temperature in THF, acetonitrile or CH_2Cl_2 does not induce any significant photochemical reaction. Only in pyridine a photoproduct was observed, although in this case also a secondary thermal reaction occurred. In order to decide whether the negligible photoreactivity in the former, less basic solvents is caused by the inertness of the excited state(s) involved or by a rapid and complete backreaction of transients to the parent cluster, the photoreactions of $[Ru_3(CO)_8(\mu\text{-}CO)_2(\alpha\text{-diimine})]$ were followed with time-resolved UV–VIS and IR spectroscopies. The studies were performed on the (sub)picosecond to nanosecond time scale. In addition, photoreactivity investigations were also performed at low temperatures and in the presence of Bu_4NBr and a radical scavenger.

(a) Time-resolved UV–VIS spectroscopy. Transient absorption (TA) spectra in the nanosecond time-domain were obtained by irradiation of clusters **2** and **3** with the 470 nm line of a tuneable Coherent Infinity XPO laser. Both in coordinating (acetonitrile, 2-MeTHF) and non-coordinating (toluene) solvents, the recorded spectra did not reveal any transient absorption bands or bleaching of the parent cluster. In order to stabilize and detect the excited state and possible photoproducts, TA spectra of cluster **2** were also recorded in a 2-MeTHF glass at 133 K. The TA spectrum at t_d = 20 ns reveals a strong bleaching around 377 and 468 nm due to the

Table 2 Main bands in the rR spectra of clusters **1** and **3**[a]

Cluster	Wavenumbers/cm^{-1}
$[Ru_3(CO)_8(\mu\text{-}CO)_2(bpy)]$ **1**	2075, 1603, 1562, 1491, 1315, 1285, 1173, 1020, 591, 571, 540, 492, 436, 356, 221
$[Ru_3(CO)_8(\mu\text{-}CO)_2(bpym)]$ **3**	2071, 1573, 1545, 1460, 1199, 1011, 568, 538, 492, 222

[a] CH_2Cl_2, $T = 293$ K, $\lambda_{exc} = 476.5$ nm.

disappearance of **2**, and transient absorptions at 413 and 600 nm. The latter absorption band is tailing to the long wavelength region, which is characteristic for α-diimine complexes in their metal-to-α-diimine excited states[29–32] and for α-diimine radical anions, provided the α-diimine bears at least one hetero-aromatic group.[18,32,33] On longer time scales (up to 1 μs) the transient species only partially regenerates the parent cluster. As for **1** and **3** on the picosecond time scale (*vide infra*), the incomplete recovery of cluster **2** in the nanosecond time domain at low temperature is ascribed to photodecomposition processes. This is inferred from the fact that no recovery of the parent cluster is observed even up to 1 ms, and from the steady-state UV–VIS spectra taken directly after the ns TA measurements. The integration and mono-exponential fitting of the transient absorption band at 600 nm resulted in a transient lifetime of 406 ± 25 ns at 133 K.

In order to observe and characterize the excited state at room temperature and to determine its kinetics, picosecond transient absorption (ps TA) spectra were recorded for cluster **1** in THF and for cluster **3** in THF and MeCN. The ps TA spectra were obtained by excitation at 505 nm and spectral changes were monitored in the wavelength region 510–700 nm. For both clusters the TA spectra at $t_d = 1$ ps show a transient absorption with a maximum at about 560 nm, its shape and position being very similar to the transient absorption band observed in the 2-MeTHF glass (*vide supra*). The transient absorption decays within 40 ps to *ca.* 50% of its initial intensity. After this interval no further spectral changes occur on the picosecond time scale. Steady-state UV–VIS spectra of the samples, taken directly after the ps TA measurements, show extensive photodecomposition. Most probably, this photodecomposition is caused by a two-photon absorption process, since no photoreaction was observed at room temperature on the ns time scale and upon continuous-wave irradiation. The photolability of both clusters under the applied experimental conditions prevented the accurate determination of the excited-state lifetime. In order to eliminate the effect of the photodecomposition, a flow-through cell was used to measure the excited-state kinetics of cluster **2** in CH_2Cl_2 and to determine the excited-state lifetime (42.9 ± 2.1 ps). In this case almost complete regeneration of the parent cluster was observed.

(b) Picosecond time-resolved infrared (ps TRIR) spectroscopy. The transient UV–VIS spectra provide only limited information about the nature of the excited state and the structure of possible photoproducts. For this reason we studied the primary events after the photoexcitation also with picosecond time-resolved infrared (ps TRIR) spectroscopy. The ps TRIR spectra were recorded for cluster **2** in CH_2Cl_2 at several pump-probe delays between 0 and 500 ps after excitation at 500 nm. Fig. 4(a) shows representative difference absorption spectra at seven selected time delays.

After excitation, the initial spectra display instantaneous bleaching of the parent *ν*(CO) bands (negative signal) superimposed on a broad, unresolved transient absorption due to the excited state of **2**. In addition, a broad transient absorption band due to bridging carbonyl(s) appears instantaneously at 1778 cm^{-1} (inset). This band is shifted to higher frequency by *ca.* 35 cm^{-1} compared to the corresponding ground-state IR band. Within the first few picoseconds the broad absorption in the terminal carbonyl region slightly shifts to higher frequency. This shift is attributed to early relaxation processes (cooling or solvation) associated with the decay of low-frequency M–C stretching and M–C–O bending vibrational modes populated upon excitation.[34–37]

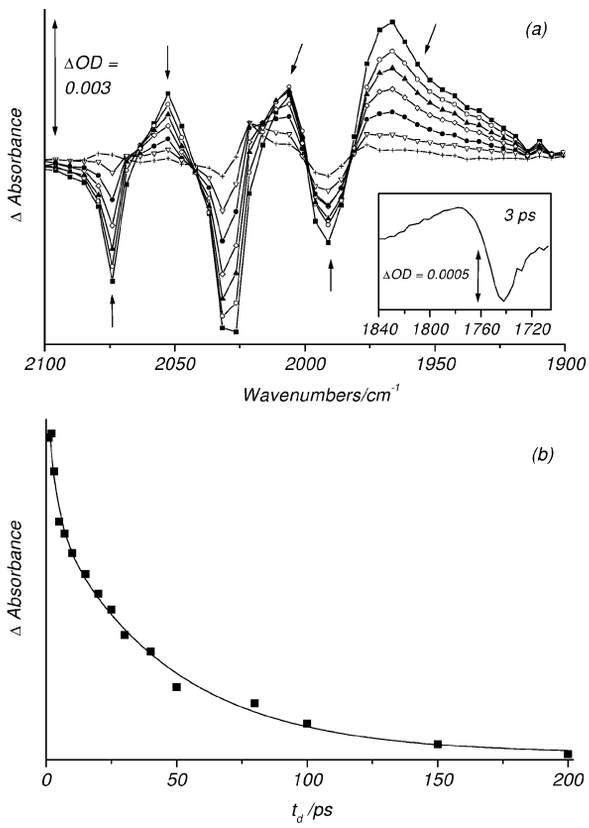

Fig. 4 (a) Difference ps TRIR spectra of cluster **2** in CH_2Cl_2 at 2 (■), 10 (○), 20 (▲), 30 (◇), 50 (●), 80 (▽) and 500 (+) ps after 500 nm excitation (*ca.* 150 fs FWHM, 5 μJ pulse^{-1}). The arrows indicate the shift of the band maxima with increasing time delay following excitation. (b) Kinetic trace representing the decay of the 1778 cm^{-1} band.

Upon further decay (≤50 ps) distinct transient absorption bands arise at 2021 and 1976 cm^{-1}, which are attributed to a photoproduct formed from the excited state. At longer time delays (up to 200 ps) the *ν*(μ-CO) band at 1778 cm^{-1} decays together with the initially observed transient in the terminal *ν*(CO) region. During this decay also the parent bleaches fade away. At early time delays (≤50 ps) the latter process is mainly ascribed to the regeneration of the cluster ground state, while at longer time delays (up to 500 ps) the contribution from the increasing overlap with the photoproduct *ν*(CO) bands dominates. At $t_d = 500$ ps after the laser pulse the initial transient absorption completely disappeared. The presence of small remaining bands at 2077w, 2053vw, 2021s, 2011m (sh), 1976m and 1962vw cm^{-1} points to the formation of a long-lived photoproduct. As the difference IR spectrum at $t_d = 500$ ps strongly resembles that of the photogenerated biradical $[^{\bullet}Os(CO)_4–Os(CO)_4–^{+}Os(CO)_2(^{i}Pr–AcPy^{\bullet-})]$ in 2-ClBu at t_d = 40 ns,[16] the long-lived photoproduct is proposed to be the open-structure biradical $[^{\bullet}Ru(CO)_4–Ru(CO)_4–^{+}Ru(CO)_2(dmb^{\bullet-})]$.

Table 3 CO-stretching frequencies of the clusters $[Ru_3(CO)_8(\mu\text{-}CO)_2(\alpha\text{-diimine})]$ and their photoproducts in various media at 293 K (unless stated otherwise)

Cluster/product	Medium	ν(CO)/cm^{-1}
1	CH_2Cl_2	2075m, 2032s, 1993vs, 1969s (sh), 1743w (br)
$\mathbf{1_{zw}(py)}$	Pyridine[a]	2065w, 2045vw, 2030w, 1986vs, 1970vs, 1929w (sh), 1900w (sh), 1884m
2	CH_2Cl_2	2074m, 2031s, 1991vs, 1967s (sh), 1741w (br)
$\mathbf{2_{zw}(Br^-)}$	THF/Bu_4NBr	2052w, 2013m, 1989m, 1957s, 1937vs, 1881m
$\mathbf{2_{zw}(Br^-)}$	PrCN/Bu_4NBr	2058w, 2015m, 1994m, 1958s, 1938vs, 1878m
3	CH_2Cl_2	2079m, 2037s, 1998vs, 1973s (sh), 1746w (br)
$\mathbf{3_{zw}(py)}$	Pyridine[a]	2065w, 2012m, 1989vs (sh), 1976vs, 1970vs (sh), 1928m (sh), 1907m (sh), 1889m

[a] T = 253 K.

Due to the strong overlap of the parent bleaches with the ν(CO) bands of the excited state in the terminal ν(CO) region, the well-separated transient ν(μ-CO) band at 1778 cm^{-1} was selected for Gaussian curve fitting. The latter band and the corresponding parent bleach were modelled as the sum of two overlapping Gaussian curves. Spectral fitting, while fixing the positions and widths of both bands, allowed the determination of the peak areas. A plot of the peak area of the 1778 cm^{-1} band against time for each time delay reveals a bi-exponential behaviour with lifetimes of 3.5 ± 1.4 ps and 45.5 ± 7.8 ps (Fig. 4(b)). In agreement with the expected sharpening of the ν(μ-CO) band at short time delays, the fast process is assigned to early relaxation processes (cooling or solvation) associated with the decay of low-frequency modes. The second, much longer lifetime is in good agreement with the value derived from the ps TA experiments (42.9 ps, *vide supra*) and is assigned to the decay of the excited state.

(c) Low-temperature photoreactions. Upon photolysis in pyridine at 253 K, clusters **1** and **3** transform into photoproducts denoted $\mathbf{1_{zw}(py)}$ and $\mathbf{3_{zw}(py)}$, respectively. Their IR data are collected in Table 3. The IR and UV–VIS spectral changes accompanying this photoreaction in the case of cluster **1** are shown in Fig. 5.

The IR and UV–VIS spectra initially show the clean formation of $\mathbf{1_{zw}(py)}$ (up to 50% conversion, Fig. 5) and $\mathbf{3_{zw}(py)}$ (up to 30% conversion). However, upon prolonged irradiation thermal and/or photochemical decomposition occurs, preventing accumulation of the photoproducts. Formation of $\mathbf{1_{zw}(py)}$ leads to a diminished UV–VIS absorption at 470 nm and the appearance of a new band at 406 nm, tailing to 650 nm. In contrast to the experiments in pyridine, continuous-wave irradiation of **1** and **3** in THF (213 K) and acetonitrile (243 K) results in negligible IR spectral changes. This behaviour demonstrates a strong influence of the coordinating ability of the solvent on the photochemistry of **1** and **3**. Photoproducts $\mathbf{1_{zw}(py)}$ and $\mathbf{3_{zw}(py)}$ are assigned as the open-structure zwitterions $[^-Ru(CO)_4\text{–}Ru(CO)_4\text{–}^+Ru(Sv)(CO)_2(\alpha\text{-diimine})]$ (Sv = pyridine), consistent with the experimental conditions required for their formation and with their IR ν(CO) patterns (Fig. 5(a) (inset), Table 3) resembling those of the solvent-stabilized zwitterions photogenerated from $[Os_3(CO)_{10}(\alpha\text{-diimine})]$ (α-diimine = bpy, bpym).[20] Attempts to characterize these compounds by ^{1}H NMR spectroscopy were unsuccessful.

(d) Photoreactions in the presence of nitrosodurene and Bu_4NBr. The presence of any radical intermediate along the photoreaction pathway of cluster **2** in THF and toluene was investigated by EPR spectroscopy in the presence of the radical scavenger nitrosodurene.[17] Upon irradiation at room temperature, stable radicals were observed that correspond to nitrosodurene spin adducts, as unambiguously revealed by their characteristic "high" g-values of 2.0073 (THF) and 2.0069 (toluene) and by hyperfine splitting (hfs) due to one ^{14}N nucleus (I = 1, 99.63%; a_N = 15.5 ± 0.1 G). These data are consistent with the localization of an odd electron in the lowest π*(NO) orbital of the spin trap. Notably, irradiation of the toluene solution in the presence of a radical scavenger at 233 K did not produce any EPR signal. Most likely, the energetic barrier for homolytic splitting of the Ru–Ru(α-diimine) bond and concomitant formation of biradicals cannot be overcome in the inert solvent at this temperature. In essence, nitrosodurene can trap only one odd electron in the biradical photoproduct (*vide supra*). We assume that this electron initially resides in the lowest π*(α-diimine) orbital of the $\{^+Ru(CO)_2(\alpha\text{-diimine})^{\bullet -}\}$ moiety.

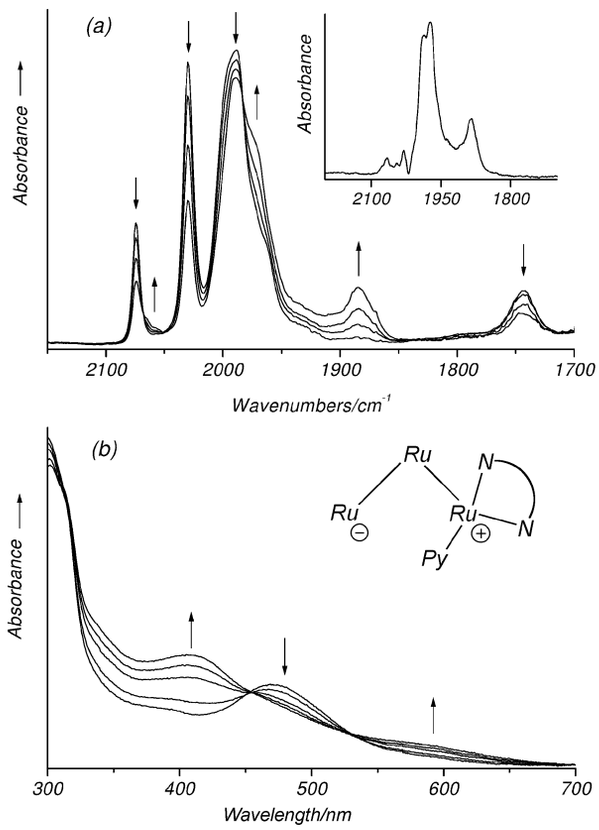

Fig. 5 IR (a) and UV–VIS (b) spectral changes accompanying photolysis of cluster **1** in pyridine at 253 K (λ_{exc} = 488 nm). Insets: (top) IR spectrum of zwitterion $\mathbf{1_{zw}(py)}$; (bottom) assumed schematic structure of $\mathbf{1_{zw}(py)}$.

Photoexcitation of **2** in the presence of Bu_4NBr results in the formation of photoproduct $\mathbf{2_{zw}(Br^-)}$ that exhibits an IR ν(CO) pattern very similar to those of zwitterions $\mathbf{1_{zw}(py)}$ and $\mathbf{3_{zw}(py)}$ formed in pyridine at 253 K. Accordingly, product $\mathbf{2_{zw}(Br^-)}$ is assigned to as the anion $[^-Ru(CO)_4\text{–}Ru(CO)_4\text{–}Ru(Br)(CO)_2(dmb)]$. It is noteworthy that $\mathbf{2_{zw}(Br^-)}$ is considerably more stable at room temperature than $\mathbf{1_{zw}(py)}$ and $\mathbf{3_{zw}(py)}$ and can be formed in high yield (up to 85% in THF and BuCN). In comparison with $\mathbf{1_{zw}(py)}$, the highest-lying ν(CO) band, which is ascribed[16] to the $\{^+Ru(L)(CO)_2(\alpha\text{-diimine})\}$ (L = pyridine or Br^-) moiety, is shifted to lower frequency in $\mathbf{2_{zw}(Br^-)}$, reflecting

Table 4 Redox potentials of clusters **1**–**3** and their reduction products.[a]

Cluster[b]	$E_{p,c}$[d]/V	ΔE_p[e]/mV	$E_{p,a}$[d]/V
1	−1.85 (irr)		+0.25 (irr)
1[c]	−1.82 (rev)	100 (100)	+0.38 (irr)
1$^{\bullet-}$[c]	−2.04	180 (100)	
[1b–1b]$^{2-}$			−1.34 (irr)
2	−1.91 (irr)		+0.28 (irr)
2[c]	−1.85 (rev)	110 (100)	+0.39 (irr)
2$^{\bullet-}$[c]	−2.15	180 (100)	
[2b–2b]$^{2-}$			−1.36 (irr)
[2b–2b]$^{2-}$[c]			−1.18 (irr)
3	−1.62	100 (100)	+0.40 (irr)
3[c]	−1.59 (rev)	100 (100)	+0.66 (irr)
3$^{\bullet-}$	−1.91	180 (100)	
3$^{\bullet-}$[c]	−1.99	220 (100)	
3b^{2-}			−1.23 (irr)
[3b–3b]$^{2-}$			−0.95 (irr)
[3b–3b]$^{2-}$[c]			−0.77 (irr)

[a] Conditions and definitions: 10^{-3} M solutions in THF (containing 10^{-1} M Bu_4NPF_6) at 293 K, unless stated otherwise; Pt disk electrode; v = 100 mV s^{-1}; redox potentials *vs.* $E_{1/2}$ (Fc/Fc$^+$); $E_{p,c}$, cathodic peak potential for reduction of parent cluster or its radical anion; $E_{p,a}$, anodic peak potential for oxidation of parent cluster or its reduction products; ΔE_p, peak-to-peak separation for a redox couple. [b] Assignments given in the main text. [c] T = 230 K. [d] Chemical reversibility and total irreversibility denoted by (rev) and (irr), respectively. [e] ΔE_p for the Fc/Fc$^+$ internal standard in parentheses.

Table 5 IR ν(CO) wavenumbers of clusters **1**–**3** and their reduction products[a]

Cluster[b]	ν(CO)/cm^{-1}
1[c]	2074m, 2030s, 1992vs, 1966s (sh), 1745w
[1b–1b]$^{2-}$[c]	2040w, 2018w, 1963vs, 1866m
[1b–1b]$^{2-}$[d]	2037w, 2012w, 1962vs, 1868m
2	2072m, 2027s, 1993s (sh), 1987vs, 1962s (sh), 1752w
[2b–2b]$^{2-}$	2037w, 2012w, 1961vs, 1867m
3	2076m, 2032s, 2000s (sh), 1994vs, 1971m (sh), 1751w
3[e]	2076m, 2032s, 2000s (sh), 1994vs, 1967m (sh), 1751w
3$^{\bullet-}$	2065m, 2024s, 1992s (sh), 1989vs, 1963m (sh), 1745w
3a$^{\bullet-}$[e]	2057m, 2014s, 1977vs, 1960m (sh), 1746w
[3b–3b]$^{2-}$	2045w, 2018w, 1967vs, 1868m
[3b–3b]$^{2-}$[e]	2044w, 2020w, 1967vs, 1871m
4^{2-}	1927s, 1866vs (br)
4^{2-}[d]	1931s, 1869vs (br)

[a] Conditions: 5 × 10^{-3} M solutions in THF (containing 10^{-1} M Bu_4NPF_6) at 293 K, unless stated otherwise; *in situ* reduction within an IR OTTLE cell.[73,74] [b] Assignments given in the main text. [c] In PrCN. [d] Chemical reduction with [Fe^I(Cp)(η^6-C_6Me_6)] performed in DME. [e] T = 240 K.

the difference in donor capacity between pyridine and the negatively charged bromide ion. Formation of **2_{zw}(Br$^-$)** is accompanied by similar UV–VIS spectral changes as observed for **1_{zw}(py)**, although the absorption bands for **2_{zw}(Br$^-$)** are slightly shifted to higher energy (370 (sh) and 586 nm for **2_{zw}(Br$^-$)** *vs.* 406 and 600 nm for **1_{zw}(py)**).

Electrochemistry

Combined cyclic voltammetric and UV–VIS–IR spectroelectrochemical studies were performed in order to describe the reduction pathways of the $[Ru_3(CO)_8(\mu\text{-}CO)_2(\alpha\text{-diimine})]$ clusters and to reveal the influence of the CO bridges on their electrochemical reactivity. The redox potentials and ν(CO) wavenumbers of clusters **1**–**3** and their reduction products are presented in Tables 4 and 5, respectively.

Reduction path of $[Ru_3(CO)_8(\mu\text{-}CO)_2(bpym)]$ (3). The cyclic voltammogram of cluster **3** in THF at room temperature (v = 100 mV s^{-1}) shows a nearly reversible one-electron reduction at $E_{1/2}$ = −1.57 V (cathodic peak R_1, I_a/I_c = 0.9; see Fig. 6(a)) that produces the corresponding radical anion **3**$^{\bullet-}$. Besides **3**$^{\bullet-}$, the cathodic process R_1 yields a small amount of a secondary product, which will be denoted as **[3b–3b]**$^{2-}$ and analyzed hereinafter. The latter product was oxidized on the reverse anodic scan at the potential $E(O_3')$.

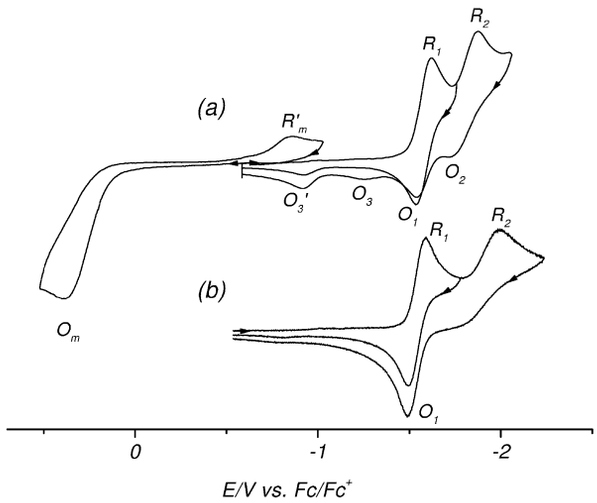

Fig. 6 Cyclic voltammograms of cluster **3** at T = 293 K (a) and T = 230 K (b). Conditions: 10^{-3} M cluster in THF/10^{-1} M Bu_4NPF_6, Pt disk microelectrode (0.42 mm^2 apparent surface area), v = 100 mV s^{-1}.

The second cathodic peak R_2 belongs to the subsequent electrochemically quasireversible one-electron reduction of **3**$^{\bullet-}$ to the corresponding dianion **3**$^{2-}$. Similar dianions are formed upon reduction of the clusters $[Os_3(CO)_{10}(\alpha\text{-diimine})]$[18,38,39] and undergo rapid metal–metal(α-diimine) bond cleavage, producing the corresponding open-structure dianions $[^-Os(CO)_4\text{–}Os(CO)_4\text{–}^-Os(CO)_2(\alpha\text{-diimine})]^{2-}$. In analogy with the reduction pathway of $[Os_3(CO)_{10}(bpym)]$,[39] closed-core dianion **3**$^{2-}$ formed upon reduction of **3**$^{\bullet-}$ is also expected to transform into the open-structure dianion $[^-Ru(CO)_4\text{–}Ru(CO)_4\text{–}^-Ru(CO)_2(bpym)]^{2-}$ (**3b**$^{2-}$), the latter being oxidized on the reverse anodic scan at the potential $E(O_3)$. This assignment is in line with the thin-layer cyclic voltammogram recorded for $[Os_3(CO)_{10}(bpym)]$ during IR spectroelectrochemical experiments.[38] On cooling to 230 K the reduction of **3** at $E(R_1)$ became chemically completely reversible (I_a/I_c = 1) and the oxidation of **[3b–3b]**$^{2-}$ was no longer observed. The second cathodic step at $E(R_2)$ again produced **3**$^{2-}$ and open-structure dianion **3b**$^{2-}$, whose oxidation at 230 K probably nearly coincides with the oxidation of **3**$^{\bullet-}$ (Fig. 6(b)). The cyclic voltammetric results thus reveal that radical anion **3**$^{\bullet-}$ is fairly stable at 293 K but can be completely stabilized only at sufficiently low temperatures.

Oxidation of **3** at the potential $E(O_m)$ is chemically irreversible, the back reduction of a secondary product being observed at the potential $E(R'_m)$.

Further evidence for the reduction pathway of cluster **3** and more information about the reduction products **3**$^{\bullet-}$ and **[3b–3b]**$^{2-}$ could be obtained from corresponding spectroelectrochemical experiments. Reduction of **3** at room temperature, followed *in situ* by IR spectroscopy, produced radical anion **3**$^{\bullet-}$ with a nearly identical IR ν(CO) pattern, the bands being shifted by *ca.* 10 cm^{-1} to smaller wavenumbers compared to the parent cluster. This shift is attributed to the increased π-back-donation from the reduced {Ru(bpym$^{\bullet-}$)} centre towards the carbonyl ligands. The EPR spectrum of **3**$^{\bullet-}$ in THF shows a clearly resolved hyperfine splitting (hfs) pattern originating from the interaction of the odd electron with four ^{14}N nuclei (I = 1, 99.63%) and two ^{1}H nuclei (I = ½, 99.99%) (see Fig. 7(a)). Simulation of the spectrum with a linewidth of 1.65 G resulted in hfs constants a_N = 2.30, 2.30, 2.60, 2.80 (± 0.1) G and a_H =

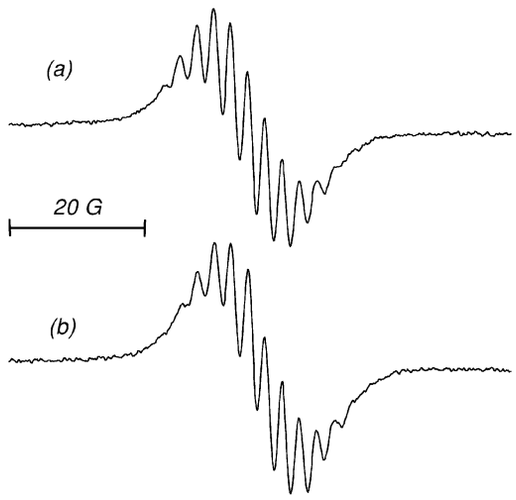

Fig. 7 EPR spectra of closely related radical anions (a) $\mathbf{3}^{\bullet-}$ (T = 293 K) and (b) $\mathbf{3a}^{\bullet-}$ (T = 240 K) in THF.

5.05, 5.15 (± 0.2) G. This result is consistent with the localization of the odd electron in the lowest-lying b_{2u} π*(bpym) molecular orbital.[27]

In the OTTLE cell, radical anion $\mathbf{3}^{\bullet-}$ converted rather slowly at room temperature to the transient species $[\mathbf{3b}–\mathbf{3b}]^{2-}$, which was only observed in small amounts. The IR ν(CO) pattern of the latter product shows a striking similarity with those of the zwitterionic and anionic photoproducts [$^{-}$Ru(CO)$_4$–Ru(CO)$_4$–$^{+}$Ru(Sv)(CO)$_2$(α-diimine)] (Sv = donor solvent) and [$^{-}$Ru(CO)$_4$–Ru(CO)$_4$–Ru(Br)(CO)$_2$(α-diimine)] ($\mathbf{1}_{zw}$**(py)** and $\mathbf{2}_{zw}$**(Br^{-})**) described above. The IR ν(CO) wavenumbers of the latter anionic photoproduct (α-diimine = dmb (**2**)) closely correspond to those of $[\mathbf{3b}–\mathbf{3b}]^{2-}$ (Tables 3 and 5, Fig. 8). This holds in particular for the band at about 1875 cm^{-1} and the highest-frequency one, which mainly represent the vibrations of the {$^{-}$Ru(CO)$_4$–Ru} and the {$^{+}$Ru(X)(CO)$_2$(α-diimine)} (X = Br^{-}) moieties,[16] respectively. This suggests that $[\mathbf{3b}–\mathbf{3b}]^{2-}$ and $\mathbf{2}_{zw}$**(Br^{-})** are isoelectronic. The observed wavenumber difference of about 10 cm^{-1} between the two most intense ν(CO) bands of $[\mathbf{3b}–\mathbf{3b}]^{2-}$ and $\mathbf{2}_{zw}$**(Br^{-})** may arise from a structural difference[38,39] between the two species. Based on these results, complex $[\mathbf{3b}–\mathbf{3b}]^{2-}$ is assigned as the cluster dimer [$^{-}$Ru(CO)$_4$–Ru(CO)$_4$–Ru(CO)$_2$(bpym)]$_2^{2-}$, with one of the Ru–Ru(bpym) bonds in each triangle open and both units linked together *via* a (bpym)Ru–Ru(bpym) bond (Scheme 1).

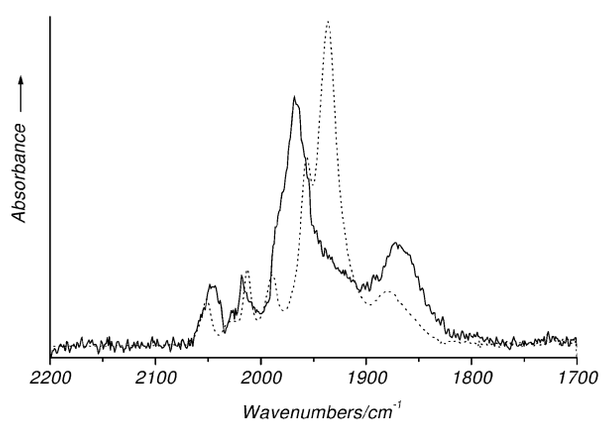

Fig. 8 IR spectra of dimer $[\mathbf{3b}–\mathbf{3b}]^{2-}$ (—) (see Scheme 1) and isoelectronic photoproduct $\mathbf{2}_{zw}$**(Br^{-})** (···) in THF at room temperature, the latter species being formed in the presence of Bu_4NBr.

Further evidence for the proposed structure of cluster dimer $[\mathbf{3b}–\mathbf{3b}]^{2-}$ is obtained from the fragmentation products obtained after reduction of $[\mathbf{3b}–\mathbf{3b}]^{2-}$ (*vide infra*). The fact that the cyclic

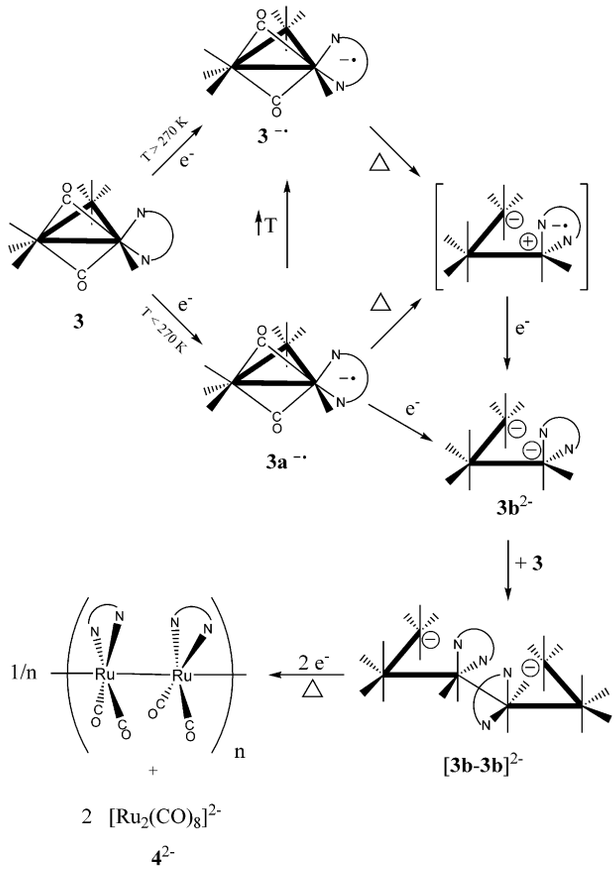

Scheme 1 Reduction path of cluster **3**.

voltammogram of **3** shows a small anodic peak due to the oxidation of $[\mathbf{3b}–\mathbf{3b}]^{2-}$ already upon scan reversal beyond the cathodic peak R_1, points to a slow thermal reaction of $\mathbf{3}^{\bullet-}$ to give its open-structure isomer, instantaneously reducible[38,39] to give open-structure dianion $\mathbf{3b}^{2-}$. The oxidation of $\mathbf{3b}^{2-}$ at $E(O_3)$ is obviously not observed upon scan reversal beyond R_1 owing to its rapid reaction with the starting material. This also explains the lacking ν(CO) bands of $\mathbf{3b}^{2-}$ during the IR spectroelectrochemical experiment at 293 K. Actually, also $[\mathbf{3b}–\mathbf{3b}]^{2-}$ is unstable at the cathode and converts to another carbonyl product absorbing at 1927s and 1866vs cm^{-1}. The ν(CO) bands (wavenumbers and intensity pattern) of the latter product closely resemble those reported for the yellow-orange dinuclear complex $[Ru_2(CO)_8]^{2-}$ ($\mathbf{4}^{2-}$) (1930 and 1866 cm^{-1} in MeCN),[40] indicating the fragmentation of the open-triangle units along the reduction pathway of $[\mathbf{3b}–\mathbf{3b}]^{2-}$. Parallel to the appearance of the ν(CO) bands at 1927 and 1866 cm^{-1}, a blue film covered the working electrode, which corresponds with the formation of another, poorly soluble product, most likely $[Ru(CO)_2(bpym)]_n$ (*vide infra*).

The reduction of cluster **3** at 240 K resulted in IR ν(CO) spectral changes similar but not identical to those observed at room temperature. Again, formation of the radical anion is reflected in the retention of the ν(CO) pattern. Most strikingly, the shift of the ν(CO) bands in the terminal CO region to smaller wavenumbers is significantly larger (*ca.* 20 cm^{-1}) than that observed at 293 K. This effect has most likely its origin in a slightly different structure of the radical anion at low temperatures, to be denoted as $\mathbf{3a}^{\bullet-}$. EPR spectra of $\mathbf{3a}^{\bullet-}$ at 240 K (Fig. 7(b)), however, reveal similar hfs constants (linewidth: 1.84 G; a_N = 2.40 (2×), 2.50 (2×) (± 0.1) G; a_H = 4.90 and 5.50 G (± 0.2) G), indicating the localization of the odd electron again in the b_{2u} π*(bpym) orbital. The combined results of the IR and EPR experiments at 240 K thus document that both radical anions $\mathbf{3}^{\bullet-}$ and $\mathbf{3a}^{\bullet-}$ are likely to be independent structural isomers. For, reduction of **3** at the intermediate temperature of

270 K in THF resulted in IR spectral changes, which initially show the formation of both isomeric forms $\mathbf{3}^{\bullet-}$ and $\mathbf{3a}^{\bullet-}$ at the same time (Fig. 9). In the course of the reduction the ν(CO) bands of $\mathbf{3}^{\bullet-}$ increased at the expense of $\mathbf{3a}^{\bullet-}$. Unfortunately, the reversibility of this interconversion process could not be proven. Upon warming up the solution of $\mathbf{3a}^{\bullet-}$ from 240 K to room temperature while keeping the electrode potential fixed, the ν(CO) bands of $\mathbf{3a}^{\bullet-}$ decreased and a small amount of $\mathbf{3}^{\bullet-}$ was formed, which then rapidly transformed into dimer $[\mathbf{3b}$–$\mathbf{3b}]^{2-}$ (Scheme 1). Analogous to the IR spectroelectrochemical experiments performed at 293 K, the reduction of $[\mathbf{3b}$–$\mathbf{3b}]^{2-}$ resulted in the appearance of ν(CO) bands at 1927s and 1866vs cm^{-1} due to dimer $\mathbf{4}^{2-}$.

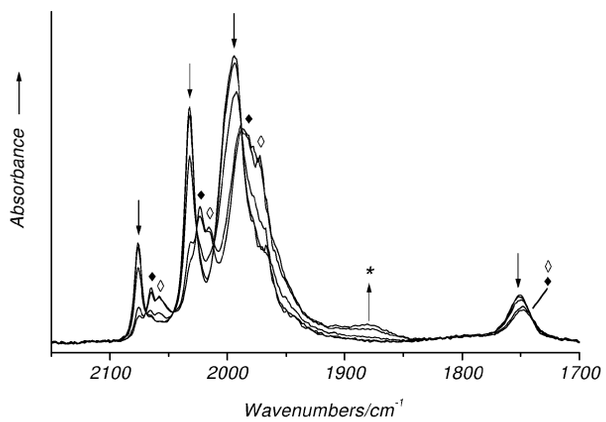

Fig. 9 IR spectral changes during the one-electron reduction of cluster **3** producing parallelly $\mathbf{3}^{\bullet-}$ (◆) and $\mathbf{3a}^{\bullet-}$ (◇). The asterisk (*) denotes a ν(CO) band due to formation of dimer $[\mathbf{3b}$–$\mathbf{3b}]^{2-}$. Conditions: THF, $T = 270$ K, *in situ* reduction within an IR OTTLE cell.[73,74]

Redox behaviour of $[Ru_3(CO)_8(\mu\text{-}CO)_2(\alpha\text{-diimine})]$ (α-diimine = bpy (1), dmb (2)). In contrast to cluster **3**, clusters **1** and **2** show in THF at room temperature chemically irreversible reduction at $E_{p,c} = -1.85$ and -1.91 V, respectively (cathodic peak R_1, see Fig. 10). For **1**, scan reversal behind R_1 showed the appearance of two anodic peaks at -1.33 V (O_3') and -0.93 V (O_4). In accordance with the results obtained for **3** and $[Os_3(CO)_{10}(bpy)]$,[39] the anodic process O_3' is assigned to the oxidation of the dimer $[^{-}Ru(CO)_4$–$Ru(CO)_4$–$Ru(CO)_2(bpy)]_2^{2-}$ ($[\mathbf{1b}$–$\mathbf{1b}]^{2-}$) (see Scheme 1). The second anodic peak O_4 is probably due to oxidation of a polymer with a structure comparable to $[Ru(CO)_2(bpy)]_n$ ($E_{p,a} = -0.99$ V *vs.* Fc/Fc^+).[41] Indirect proof for the formation of such polymers upon reduction of $[Ru_3(CO)_8(\mu\text{-}CO)_2(\alpha\text{-diimine})]$ was obtained from IR spectroelectrochemical experiments (*vide infra*). For cluster **2**, a similar reverse anodic sweep was observed.

On lowering the temperature to 230 K, the reductions of **1** and **2** at $E(R_1)$ turned into chemically and electrochemically reversible ($v = 100$ mV s^{-1}) one-electron processes. This step yields the corresponding radical anions $\mathbf{1}^{\bullet-}$ and $\mathbf{2}^{\bullet-}$. The cathodic peak R_2 in Fig. 10 then belongs to the subsequent partly chemically reversible one-electron reduction of $\mathbf{1}^{\bullet-}$ and $\mathbf{2}^{\bullet-}$, producing ultimately the open-structure dianions $\mathbf{1b}^{2-}$ and $\mathbf{2b}^{2-}$. In contrast to the scans at room temperature, these dianions are fairly stable on the CV time scale at 230 K. Their oxidation nearly coincides with the oxidation of $\mathbf{1}^{\bullet-}$ and $\mathbf{2}^{\bullet-}$, respectively (see Fig. 10(b)), and becomes better resolved upon slightly raising the temperature. As the zero-electron coupling reaction of $\mathbf{1b}^{2-}$ with parent cluster **1** is hindered at 230 K, no oxidation waves due to $[\mathbf{1b}$–$\mathbf{1b}]^{2-}$ and the polymer $[Ru(CO)_2(bpy)]_n$ are observed on the reverse scan. However, similar to $[Os_3(CO)_{10}(dmb)]$, dianion $\mathbf{2b}^{2-}$ is more reactive, the oxidation of dimer $[\mathbf{2b}$–$\mathbf{2b}]^{2-}$ at 230 K being clearly visible at $E_{p,a} = -1.18$ V. The cyclic voltammetric results prove that the radical anions $\mathbf{1}^{\bullet-}$ and $\mathbf{2}^{\bullet-}$ are very unstable at 293 K and readily transform to the open-structure dianions, $\mathbf{1b}^{2-}$ and $\mathbf{2b}^{2-}$, respectively, probably *via* the open-structure radical transient $[^{-}Ru(CO)_4$–$Ru(CO)_4$–$^{+}Ru(CO)_2(\alpha\text{-diimine}^{\bullet-})]$ (see Scheme 1). The latter dianions could also not be observed at room temperature due to their rapid nucleophilic attack at the yet non-reduced parent clusters, converting into dimeric and, subsequently, polymeric reduction products.

The irreversible character of the reduction of clusters **1** and **2** at 293 K on the CV time scale was further confirmed by IR spectroelectrochemistry in THF at 293 and 240 K. At both temperatures radical anions $\mathbf{1}^{\bullet-}$ and $\mathbf{2}^{\bullet-}$ are not detectable. Instead, reduction of **1** and **2** resulted in the formation of dimers $[\mathbf{1b}$–$\mathbf{1b}]^{2-}$ and $[\mathbf{2b}$–$\mathbf{2b}]^{2-}$ (Table 5), respectively, which rapidly decomposed into the dinuclear complex $[Ru_2(CO)_8]^{2-}$ ($\mathbf{4}^{2-}$), as indicated by the appearance of ν(CO) bands at 1927s and 1867vs cm^{-1}. Similar to the results for cluster **3**, the formation of $\mathbf{4}^{2-}$ was accompanied by the appearance of a blue film at the working electrode and in its vicinity, characteristic for the formation of poorly soluble polymers $[Ru(CO)_2(\alpha\text{-diimine})]_n$ (α-diimine = bpy, dmb).[42,43] The dimer $[\mathbf{1b}$–$\mathbf{1b}]^{2-}$ was also formed upon chemical reduction of **1** with one equivalent of $[Fe^{I}(Cp)(\eta^6\text{-}C_6Me_6)]$ in DME (Table 5). Addition of a second equivalent caused a decrease of the ν(CO) bands of $[\mathbf{1b}$–$\mathbf{1b}]^{2-}$ to *ca.* 50% of their initial intensity and appearance of a new ν(CO) band at 1931s cm^{-1} due to the formation of $\mathbf{4}^{2-}$. In addition, a weak ν(CO) band at 1882 cm^{-1} is observed, which is attributed, in analogy with supplementary results for $[Ru(CO)_2(dmb)(I)_2]$‡, to the polymer $[Ru(CO)_2(bpy)]_n$.

Molecular orbital calculations

Density functional theory (DFT) and time-dependent DFT (TD-DFT) calculations were performed in order to obtain more insight into the bonding properties of the clusters

‡ Electrochemical two-electron reduction of the mononuclear complexes *trans*(Cl)-$[Ru(CO)_2(\alpha\text{-diimine})(Cl)_2]$ (α-diimine = bpy, dmb) is known to result ultimately in the generation of the corresponding polymers $[Ru(CO)_2(\alpha\text{-diimine})]_n$.[42,43] The formation of similar polymeric products upon reduction of the analogous bpym complex has not been reported so far. In order to confirm the electrochemical formation of polymers in the latter case, IR spectroelectrochemical experiments were performed on the dinuclear complex $[\{Ru(CO)_2(I)_2\}_2(\mu\text{-bpym})]$, using $[Ru(CO)_2(dmb)(I)_2]$ as a reference.

The cyclic voltammograms of $[Ru(CO)_2(dmb)(I)_2]$ and $[\{Ru(CO)_2(I)_2\}_2(\mu\text{-bpym})]$ in THF at room temperature show a broad, chemically irreversible reduction at $E_{p,c} = -1.96$ V for $[Ru(CO)_2(dmb)(I)_2]$ and -1.59 V for $[\{Ru(CO)_2(I)_2\}_2(\mu\text{-bpym})]$, respectively. In PrCN this reduction process is split into two clearly separated cathodic steps, resulting in chemically irreversible reductions at $E_{p,c} = -1.76$ and -1.90 V for $[Ru(CO)_2(dmb)(I)_2]$ and $E_{p,c} = -1.44$ and -1.55 V for $[\{Ru(CO)_2(I)_2\}_2(\mu\text{-bpym})]$. Upon spectroelectrochemical detection, reduction of $[Ru(CO)_2(dmb)(I)_2]$ in THF initially resulted in the appearance of small ν(CO) bands at 2013 and 1938 cm^{-1} that are assigned to the dimer $[Ru(CO)_2(dmb)(I)]_2$, possessing a (dmb)Ru–Ru(dmb) bond.[44] Going to more negative potentials the ν(CO) bands of the starting complex and the dimer disappeared and no remaining product bands were observed. Instead, the working electrode was covered with a blue film that was insoluble in THF. In PrCN, formation of the dimer was no longer observed. Instead, reduction of $[Ru(CO)_2(dmb)(I)_2]$ resulted in the appearance of ν(CO) bands at 1964 and 1884 cm^{-1} that are ascribed to the polymer $[Ru(CO)_2(dmb)]_n$. Reduction of this polymer at a more negative electrode potential resulted in ν(CO) bands at 1912 and 1845 cm^{-1} that accordingly are assigned to the dmb-reduced form of the polymer. Reduction of $[\{Ru(CO)_2(I)_2\}_2(\mu\text{-bpym})]$ in THF initially resulted in the appearance of small ν(CO) bands at 2040 and 1986 cm^{-1}. At more negative potentials this product converted into the dimer $[Ru(CO)_2(bpym)(I)]_2$ (2023 and 1949 cm^{-1}), having its ν(CO) bands at slightly larger wavenumbers than observed for $[Ru(CO)_2(dmb)(I)]_2$. Similarly to $[Ru(CO)_2(dmb)(I)_2]$ in THF, the reduction of $[Ru(CO)_2(bpym)(I)]_2$ did not result in any observable product bands. In PrCN, initial reduction of $[\{Ru(CO)_2(I)_2\}_2(\mu\text{-bpym})]$ resulted in the formation of the same intermediates as observed in THF. Further reduction of the dimer $[Ru(CO)_2(bpym)(I)]_2$ in PrCN, however, resulted in the appearance of small ν(CO) bands at 1960 and 1900 cm^{-1} that, in accordance with the results for $[Ru(CO)_2(dmb)(I)_2]$, are ascribed to the polymer $[Ru(CO)_2(bpym)]_n$.

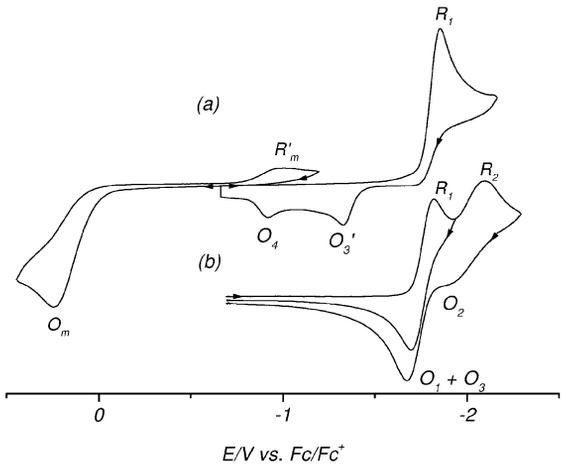

Fig. 10 Cyclic voltammograms of cluster **1** at $T = 293$ K (a) and $T = 230$ K (b). Conditions: 10^{-3} M cluster in THF/10^{-1} M Bu_4NPF_6, Pt disk microelectrode (0.42 mm² apparent surface area), $v = 100$ mV s^{-1}.

$[Ru_3(CO)_8(\mu\text{-}CO)_2(\alpha\text{-diimine})]$ and to assign their lowest-energy electronic transitions. The available crystal structure[45] of the cluster $[Ru_3(CO)_8(\mu\text{-}CO)_2(bpy)]$ (**1**) provided a starting geometry for the calculations. Three possible isomers of this cluster are depicted in Fig. 11. Cluster **1′** has all carbonyl ligands in terminal positions and the bpy ligand coordinated in the favored equatorial–axial mode. Isomer **1″**, very similar to cluster **1**, exhibits two carbonyl ligands bridging a Ru–Ru(bpy) bond. The bridging carbonyls give rise to heptacoordination of the Ru1 and Ru3 centres and a different arrangement of the bpy ligand relative to the Ru_3 plane. The inter-ring C–C bond of the bpy ligand in **1″** lies perpendicular to the plane of the cluster core. In the third isomer, **1‴**, the bridging carbonyls span the bond between the Ru centres not binding the α-diimine ligand.

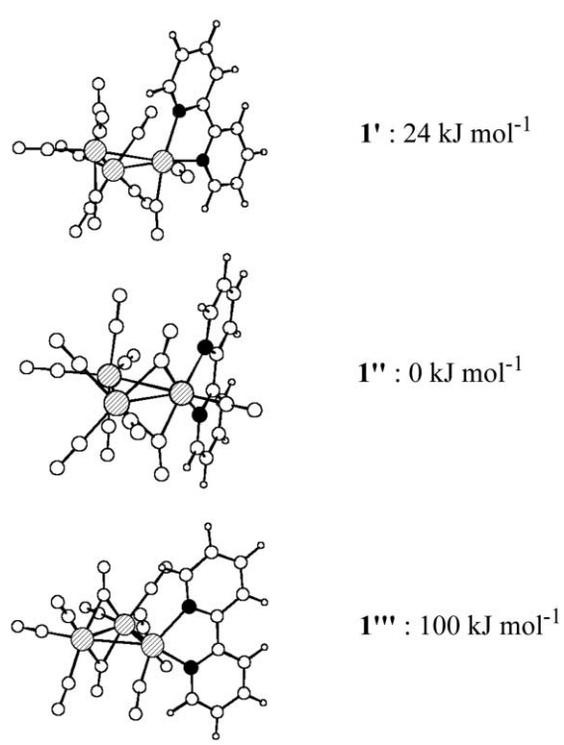

Fig. 11 Optimized geometries and relative energies (in kJ mol^{-1}) of the structural models **1′**, **1″** and **1‴**.

The energies of the optimized isomers show that isomer **1″** with the two CO bridges, as in the crystal structure of cluster **1**, is the most stable one (24 kJ mol^{-1} relative to the terminal isomer and 100 kJ mol^{-1} relative to the second bridged isomer). The coordination of the α-diimine ligand to Ru leads to an increase of the electronic density at this metal centre, and therefore to stronger π-back-donation to the carbonyls. A structure with bridges becomes more favourable, if the bridging carbonyls bind the same Ru atom, as in the experimental structure of cluster **1**. The structure **1′** with terminal carbonyls comes next, followed, at a very high energy by **1‴**, the structure with the CO bridges in the "wrong" position. The geometry of cluster **1″** is in good agreement with the experimental structure (Fig. 11, Table 6). The ground state calculations of **1″** therefore afforded the composition of the molecular orbitals that also applies for **1**. The contributions of the relevant atoms to the frontier orbitals are given in Table 7. Three-dimensional Molekel plots[46] are depicted in Fig. 12 for the three highest occupied molecular orbitals (HOMO, HOMO−1 and HOMO−2) and the lowest unoccupied molecular orbital (LUMO).

Table 6 Comparison of selected calculated bond lengths [Å] and angles [°] in cluster **1″** with the experimental[45] crystallographic data

Bond[a]	Calc.	Exptl.	Angle[a]	Calc.	Exptl.
Ru1–Ru2	2.94	2.86	Ru1–Ru2–Ru3	56.94	57.97
Ru1–Ru3	2.79	2.76	Ru1–Ru3–Ru2	62.26	61.36
Ru2–Ru3	2.90	2.84	Ru2–Ru1–Ru3	60.81	60.67
Ru1–N1	2.20	2.19	Ru1–C1–Ru3	82.79	82.34
Ru1–N2	2.20	2.19	Ru1–C2–Ru3	84.19	84.06
Ru1–C1	1.96	1.96	Ru3–Ru1–N1	135.0	135.95
Ru3–C1	2.24	2.22	Ru3–Ru1–N2	136.1	136.83
Ru1–C2	2.02	2.03	N1–Ru1–N2	74.13	73.48
Ru3–C2	2.13	2.09	$N1–C_2–C_{2'}$	115.8	115.4
$N1–C_2$	1.36	1.34	$N2–C_{2'}–C_2$	115.7	116.0
$N2–C_{2'}$	1.36	1.33			
$C_2–C_{2'}$	1.47	1.46			

[a] See Fig. 1.

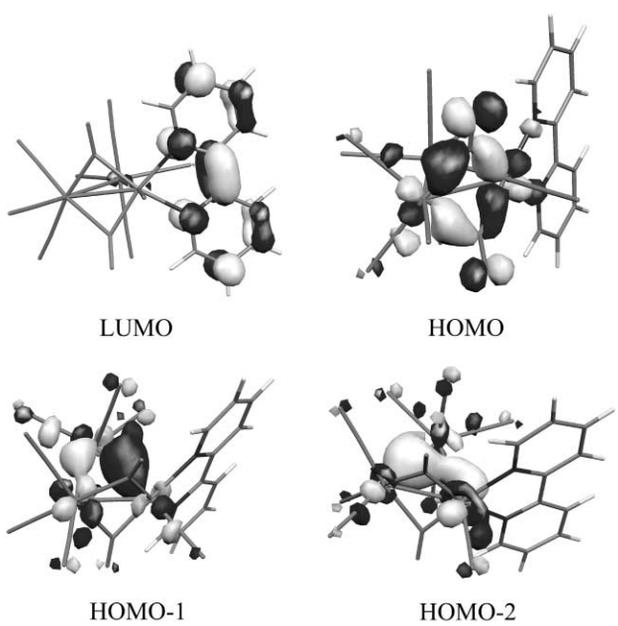

Fig. 12 3D representations of four frontier orbitals of $[Ru_3(CO)_8(\mu\text{-}CO)_2(bpy)]$ (**1″**).

The HOMO of cluster **1″** (and **1**) is mainly localized on the Ru1–$(\mu\text{-}CO)_2$–Ru3 moiety. Its character is π-bonding between Ru and the bridging carbonyl ligands, π(Ru/μ-CO), but also antibonding between the same Ru atoms, π*(Ru–Ru). The three ruthenium centres participate in the HOMO−1 and HOMO−2. The HOMO−1 involves σ-bonding interactions between Ru1 and Ru2 (dominant) and between Ru2 and Ru3, while the HOMO−2 is bonding with regard to the entire metal

Table 7 Characters and one-electron energies (E) of selected frontier orbitals of $[Ru_3(CO)_8(\mu\text{-}CO)_2(bpy)]$, as calculated by the ADF/BP method (L = LUMO, H = HOMO)

MO		E/eV	Contribution (%)					
			Ru1[a]	Ru2[a]	Ru3[a]	bpy	CO	μ-CO
106a	L+2	−3.01	2	1	1	88	1	3
105a	L+1	−3.24	22	9	13	11	20	15
104a	**L**	**−3.76**	**2**	**4**	**1**	**85**	**3**	**1**
103a	**H**	**−5.08**	**19**	**1**	**24**	**4**	**11**	**36**
102a	H−1	−5.39	15	36	12	2	28	2
101a	H−2	−5.58	21	19	18	6	27	1
100a	H−3	−6.13	42	2	20	2	10	20

[a] See Fig. 1.

Table 8 Lowest-energy singlet excitation energies (E) and oscillator strengths (O.S.) for $[Ru_3(CO)_8(\mu\text{-}CO)_2(bpy)]$ (**1″**), as calculated by TD-DFT

Transition	Composition (%)	E/eV	λ/nm	λ_{max}[a]/nm	10^3 (O.S.)
1	99 (H⟶L)	1.34	926	[b,c]	0.003
2	88 (H−1⟶L) 9 (H−2⟶L)	1.71	727	[b,c]	4.1
3	88 (H−2⟶L) 7 (H−1⟶L)	1.97	629	473	46
4	54 (H⟶L+2) 45 (H⟶L+1)	2.03	610	[b]	0.24
5	52 (H⟶L+1) 46 (H⟶L+2)	2.14	579	[b]	0.68
6	100 (H⟶L+3)	2.29	542	[b]	0.065
7	61 (H−1⟶L+2) 35 (H−3⟶L)	2.38	520	[b]	0.81
8	59 (H−3⟶L) 28 (H−1⟶L+2)	2.41	514	[b,d]	20
9	82 (H−2⟶L+1) 10 (H−1⟶L+1)	2.44	508	[b,d]	6.9
10	58 (H−1⟶L+1) 10 (H−2⟶L+2) 9 (H−2⟶L+1) 9 (H−1⟶L+2)	2.53	490	[b,d]	35

[a] Absorption maxima for $[Ru_3(CO)_8(\mu\text{-}CO)_2(bpy)]$ in toluene at 298 K. [b] Non-resolved. [c] Corresponds to tailing absorption between 550 and 650 nm (see Fig. 2). [d] Absorption band with maximum at 388 nm in THF and MeCN (see Fig. 2).

core and will be denoted as $\sigma(Ru_3)$. The LUMO mainly consists of the lowest π*(bpy) orbital, while the LUMO+1 (not shown) is delocalized over the ruthenium carbonyl core. Based on the compositions of the frontier orbitals, the HOMO–LUMO transition can be described as having a predominant π(Ru/μ-CO)-to-π*(α-diimine) character.

The excitation energies and the oscillator strengths of the low-lying electronic transitions of isomer **1″**, calculated using TD-DFT, are presented in Table 8.

Discussion

Molecular structure of $[Ru_3(CO)_8(\mu\text{-}CO)_2(\alpha\text{-diimine})]$

The presence of bridging carbonyl ligands in the clusters $[Ru_3(CO)_8(\mu\text{-}CO)_2(\alpha\text{-diimine})]$ (α-diimine = bpy (**1**), dmb (**2**), bpym (**3**)) is evidenced by their IR spectra and the reported crystal structure for cluster **1**.[45] Comparison of this crystal structure with that of the related cluster $[Os_3(CO)_{10}(bpy)]$[47] reveals some interesting differences, arising from the position of the α-diimine ligand and the different coordination environment of two metal centres. In both compounds, the α-diimine ligand is only bound to a single metal centre in a chelating fashion. However, while in the triosmium cluster 2,2′-bipyridine coordinates with one nitrogen axial and the other one in equatorial position, in cluster **1** the bpy ligand must reorient in order to get both donor nitrogens bound approximately *trans* to the bridging carbonyl groups that are stronger π-acceptors than the terminal carbonyls. There is some difference in the average metal–metal bond length in cluster **1** (2.816(2) Å) compared to its osmium analogue (2.875(3) Å), which is not surprising considering the different coordination geometry of Ru and Os in their corresponding clusters. This difference mainly results from the significant shortening of the CO-bridged Ru–Ru distance (2.757(1) Å) compared to the non-bridged Ru–Ru and Ru–Ru(bpy) bonds (2.836(1) and 2.855(1) Å, respectively); therefore it does not make sense to compare the average bond lengths. Indeed, the average metal–metal bond lengths in the parent unsubstituted clusters $[M_3(CO)_{12}]$ (M = Ru, Os) are not significantly different: replacement of osmium by ruthenium only results in a rather small contraction of the metal–metal bonds from 2.8771(9) Å for Os[48] to 2.8541(7) Å for Ru.[49] Similarly, the non-bridged Ru–Ru bonds in **1** are comparable to Os–Os bonds in $[Os_3(CO)_{10}(bpy)]$. Coordination of the donor α-diimine ligand to $[Ru_3(CO)_{12}]$ increases the electron density at the ruthenium centres sufficiently to induce fromation of the CO bridges. On the other hand, the influence of the α-diimine coordination on the metal–metal bond lengths in $[M_3(CO)_{12}]$ (M = Ru, Os) is limited (2.877 *vs.* 2.875 Å for Os; 2.8541(7) Å *vs.* 2.836(1) and 2.855(1) Å for Ru), except for the Ru–Ru bond spanned by the CO groups (2.757(1) Å).

In solution, these CO bridges are no longer localized between two specific Ru centres, but are expected to bridge across both Ru–Ru(α-diimine) bonds in a dynamic equilibrium. Both Ru–Ru(α-diimine) bonds will therefore be shortened and strengthened. This will influence the redox and photochemical reactivity of the clusters $[Ru_3(CO)_8(\mu\text{-}CO)_2(\alpha\text{-diimine})]$ to a large extent, as the formation of open-structure products will be far less efficient than in the case of the analogous triosmium clusters.

Stability of the radical anions

From the DFT results (Table 7) it is clear that the LUMO of the clusters $[Ru_3(CO)_8(\mu\text{-}CO)_2(\alpha\text{-diimine})]$ is strongly localized in the lowest π*(α-diimine) orbital. Single occupation of this orbital upon one-electron reduction is therefore expected to result in α-diimine-localized radical anions. The EPR spectra confirm this and the (spectro)electrochemical data show that the radical anions $[Ru_3(CO)_8(\mu\text{-}CO)_2(\alpha\text{-diimine})]^{\bullet-}$ are fairly stable. A comparison of the reduction potentials of the studied triruthenium clusters (at 230 K) reveals that the π-acceptor capacity of the coordinated α-diimine increases in the order dmb ($E_{1/2}$ (**2**) = −1.77 V) < bpy ($E_{1/2}$ (**1**) = −1.80 V) ≪ bpym ($E_{1/2}$ (**3**) = −1.54 V). In accordance with this trend, radical anion $\mathbf{3}^{\bullet-}$ can even be detected at room temperature by IR spectroscopy (*i.e.* on the time scale of minutes) whereas radical anions $\mathbf{1}^{\bullet-}$ and $\mathbf{2}^{\bullet-}$ are only observable by cyclic voltammetry. At room temperature, both $\mathbf{1}^{\bullet-}$ and $\mathbf{2}^{\bullet-}$ undergo a fast follow-up chemical reaction with a low activation energy. Differently from the radical anion $[Os_3(CO)_{10}(bpym)]^{\bullet-}$, which is unstable above 213 K,[39] the radical anion $\mathbf{3a}^{\bullet-}$ is completely stable already at 240 K, emphasizing the better π-acceptor capability of the bridging CO ligands.

The most striking result upon the one-electron reduction of cluster **3** is the observation of two different isomeric forms for its radical anion, *viz*. $\mathbf{3}^{\bullet-}$ and $\mathbf{3a}^{\bullet-}$. Consistent with their EPR spectra, the added electron in both cases resides in the lowest π*(bpym) orbital. However, the IR spectra of the radical anions (Table 5) show a distinct difference in their *ν*(CO) wavenumbers (*ca*. 10 cm^{-1}) and, hence, in the π-back-donation to the carbonyl ligands. Importantly, the spectroelectrochemical experiments prove that the IR *ν*(CO) patterns observed at room temperature and 240 K indeed belong to two independent species. The one-electron reduction of **3** at 240 K produces radical anion $\mathbf{3a}^{\bullet-}$ with the preserved structure of the parent cluster, while at room temperature a thermodynamically more stable derivative $\mathbf{3}^{\bullet-}$ is formed. This is in line with the IR spectroelectrochemical experiment at 270 K where the reduction of **3** initially results in the formation of both radical anions, but in the further course of the reduction $\mathbf{3a}^{\bullet-}$ gradually converts into $\mathbf{3}^{\bullet-}$. The radical anions may slightly differ, for instance, in the orientation of the α-diimine ligand with respect to the Ru_3 core, which concomitantly influences the donation of electron density from the reduced bpym ligand to the cluster core and, hence, also the Ru–to–CO π-back-bonding. The barrier for conversion of $\mathbf{3a}^{\bullet-}$ into $\mathbf{3}^{\bullet-}$ is supposed to result from solvent interactions that prevent reorientation of the α-diimine ligand at temperatures below 260 K. Convincing evidence for this hypothesis might be obtained from interconversion experiments where solutions containing $\mathbf{3}^{\bullet-}$ or $\mathbf{3a}^{\bullet-}$ are cooled down or warmed up, respectively. Indeed, $\mathbf{3a}^{\bullet-}$ was found to convert to $\mathbf{3}^{\bullet-}$ upon raising the temperature. Unfortunately, the reverse experiment was not decisive since $\mathbf{3}^{\bullet-}$ cannot be completely stabilized at room temperature on the time scale of the spectroelectrochemical experiment.

Electrochemical formation of open-structure products

The irreversible reduction of **1** and **2** at room temperature points to a one-electron α-diimine-localized process that is followed by a fast chemical reaction of the primary reduction products $\mathbf{1}^{\bullet-}$ and $\mathbf{2}^{\bullet-}$ (opening of a Ru–Ru(α-diimine) bond) and by the concomitant consumption of a second electron to produce the corresponding open-structure dianions. The latter compounds, however, undergo at ambient temperature a coupling reaction with the parent cluster to give corresponding dianionic dimers (Scheme 1). Similar zero-electron coupling reactions occur commonly, for example between mononuclear complexes $[Mn(Sv)(CO)_3(bpy)]^+$ (Sv = THF, MeCN) and two-electron-reduced $[Mn(CO)_3(bpy)]^-$, producing the dimer $[Mn(CO)_3(bpy)]_2$.[50] In this respect, the reactive primary reduction products $\mathbf{1}^{\bullet-}$ and $\mathbf{2}^{\bullet-}$ compare well with the radical anions $[M_3(CO)_{12}]^{\bullet-}$ (M = Ru, Os)[51,52] that are short-lived ($[Ru_3(CO)_{12}]^{\bullet-}$ has a half-life $t_{1/2} < 10^{-6}$ s in CH_2Cl_2) and convert to dianions $[M_3(CO)_{10}(\mu\text{-}CO)]^{2-}$ *via* an open-structure transient. Also in this case the cleavage of a M–M bond in the radical anion $[M_3(CO)_{12}]^{\bullet-}$ induces formation of the doubly reduced cluster at the applied reduction potential of $[M_3(CO)_{12}]$.

In contrast to the cluster $[Os_3(CO)_{10}(bpym)]$,[38,39] for which the open-structure dianion could be stabilized in butyronitrile on the spectroelectrochemical time scale, the open-structure dianion $\mathbf{3b}^{2-}$ could only be observed by cyclic voltammetry at moderate scan rates. This points to negligible solvent coordination and low activation energy for the subsequent coupling reaction with the parent cluster to form $[\mathbf{3b}\text{–}\mathbf{3b}]^{2-}$. The latter compound, although observable, transforms readily in the course of the spectroelectrochemical experiment into $[Ru_2(CO)_8]^{2-}$ ($\mathbf{4}^{2-}$) and a poorly soluble polymer consisting of $\{Ru(CO)_2(\alpha\text{-diimine})\}$ units. The above results show that the electrochemically induced cleavage of the Ru–Ru(α-diimine) bond results in the formation of far more reactive open-structure reduction products than observed upon reduction of $[Os_3(CO)_{10}(\alpha\text{-diimine})]$.

The assignment of polymers $[Ru(CO)_2(\alpha\text{-diimine})]_n$ as the ultimate products obtained upon reduction of $[Ru_3(CO)_8(\mu\text{-}CO)_2(\alpha\text{-diimine})]$, is mainly based on a comparison with the reduction paths of the mononuclear complexes $[Ru(CO)_2(dmb)(I)_2]$ and $[\{Ru(CO)_2(I)_2\}_2(\mu\text{-bpym})]$. Two-electron reduction of $[Ru(CO)_2(dmb)(I)_2]$ produces the polymer $[Ru(CO)_2(dmb)]_n$, possessing *ν*(CO) bands at 1964 and 1884 cm^{-1} (*vide supra*). In a similar way, the electrochemical reduction of the mononuclear complexes *trans*(Cl)–$[M(CO)_2(bpy)(Cl)_2]$ (M = Ru, Os) is known to result in the generation of polymers $[M(CO)_2(bpy)]_n$, with *ν*(CO) bands at similar wavenumbers (*viz*. $[Ru(CO)_2(bpy)]_n$ *ν*(CO): 1966 and 1885 cm^{-1} in CsI).[53] The interest in these open-chain polymers mainly derives from their electrocatalytic activity towards reduction of carbon dioxide.[41,43,54] In order to reveal electrochemical polymer formation for a structurally related Ru/bpym complex, IR spectroelectrochemical experiments were performed on $[\{Ru(CO)_2(I)_2\}_2(\mu\text{-bpym})]$. The ultimate reduction product in this case closely resembles the polymer $[Ru(CO)_2(dmb)]_n$, which supports its assignment as $[Ru(CO)_2(bpym)]_n$. Importantly, both polymers $[Ru(CO)_2(\alpha\text{-diimine})]_n$ (α-diimine = dmb, bpym) are insoluble in THF and their formation in this solvent was indicated by the appearance of a characteristic blue film at the working electrode and in its vicinity.

Electrochemical reduction of the clusters $[Ru_3(CO)_8(\mu\text{-}CO)_2(\alpha\text{-diimine})]$ ultimately results in the formation of similar blue films as observed for $[Ru(CO)_2(dmb)(I)_2]$ and $[\{Ru(CO)_2(I)_2\}_2(\mu\text{-bpym})]$, assigned again to polymers $[Ru(CO)_2(\alpha\text{-diimine})]_n$. Consistent with this assignment, efficient electrocatalytic reduction of carbon dioxide was observed upon bulk electrolysis of **1** in THF saturated with CO_2.[24] Apart from the polymer films, reduction of the open-structure dimers $[^-Ru(CO)_4\text{–}Ru(CO)_4\text{–}Ru(CO)_2(\alpha\text{-diimine})]_2^{2-}$ (α-diimine = bpy, dmb, bpym) (Scheme 1) results in the production of a compound with *ν*(CO) bands at 1927 and 1866 cm^{-1}, independent of the α-diimine ligand used. In accordance with the literature,[40] the CO-stretching bands are attributed to the dinuclear complex $[Ru_2(CO)_8]^{2-}$ ($\mathbf{4}^{2-}$). The formation of the latter complex suggests that upon reduction of the open-structure cluster dimers fragmentation of the open-triangle units takes place. Apart from $\mathbf{4}^{2-}$, this process also results in dinuclear fragments $\{Ru(CO)_2(\alpha\text{-diimine})\}_2$ that readily link together to form the polymeric chain $[Ru(CO)_2(\alpha\text{-diimine})]_n$. Observation of $\mathbf{4}^{2-}$ therefore also supports the assignment of polymers $[Ru(CO)_2(\alpha\text{-diimine})]_n$ as one of the ultimate reduction products of the clusters $[Ru_3(CO)_8(\mu\text{-}CO)_2(\alpha\text{-diimine})]$.

Mechanism of the electrochemical Ru–Ru bond cleavage

The one-electron reduction of $[Ru_3(CO)_8(\mu\text{-}CO)_2(\alpha\text{-diimine})]$ is evidently localized on the α-diimine ligand, in agreement with the EPR and IR spectra of $\mathbf{3}^{\bullet-}$. The heterolytic cleavage of the Ru–Ru(α-diimine) bond in $[Ru_3(CO)_8(\mu\text{-}CO)_2(\alpha\text{-diimine})]^{\bullet-}$ has its origin in strong polarization of this bond *via* charge "leakage" from the reduced α-diimine ligand,[55] the degree of which is mainly controlled by its π-acceptor ability. The basicity of the α-diimine radical anion is significantly increased on going from bpym to bpy and dmb, as reflected in the more negative reduction potential in this series. In the same order, the unpaired electron becomes more delocalized over the Ru–(α-diimine) chelate bond which will, in turn, considerably polarize the Ru–Ru(α-diimine$^{\bullet-}$) σ-bond and cause its heterolytic cleavage into $Ru^- \cdots Ru^+(\alpha\text{-diimine}^{\bullet-})$. A similar dependence on the α-diimine ligand was reported for the one-electron reduction of the complexes $[(CO)_5MnRe(CO)_3(\alpha\text{-diimine})]$, producing stable $[Mn(CO)_5]^-$ and reactive radicals $[Re^+(CO)_3(\alpha\text{-diimine}^{\bullet-})]$.[56]

The influence of the bridging CO ligands on the electrochemical reactivity of the clusters $[Ru_3(CO)_8(\mu\text{-}CO)_2(\alpha\text{-diimine})]$ is clearly reflected in the stability of the corresponding radical anions. Whereas $\mathbf{3}^{\bullet-}$ can already be completely stabilized on the time scale of the spectroelectrochemical experiments at 240 K, the analogous triosmium cluster required a significantly lower temperature (213 K) to prevent cleavage of the metal–metal(α-diimine$^{\bullet-}$) bond. The same holds for the radical anions $\mathbf{1}^{\bullet-}$ and $\mathbf{2}^{\bullet-}$ observed on the CV time scale, that are also considerably more stable than $[Os_3(CO)_{10}(bpy)]^{\bullet-}$.[38,39] Both results indicate that the energetic barrier for the metal–metal bond cleavage in $[Os_3(CO)_{10}(\alpha\text{-diimine})]^{\bullet-}$ is significantly lower. This is explained by the presence of the bridging CO ligands in the case of $[Ru_3(CO)_8(\mu\text{-}CO)_2(\alpha\text{-diimine})]$, that stabilize the anionic structure through their better π-acceptor capabilities. The Ru–$\{C(O)\}_2$–Ru moiety is strongly held together by means of the Ru–C bonding interactions, making the Ru–Ru bond cleavage less favourable. In addition, the presence of strong π-acceptor CO bridges also reduces the polarization of the Ru–Ru(α-diimine) bond to such an extent that it becomes less prone to heterolytic cleavage. In contrast to the increased stability of the radical anions $[Ru_3(CO)_8(\mu\text{-}CO)_2(\alpha\text{-diimine})]^{\bullet-}$, the open-structure products formed along the reduction path are less stable than their triosmium analogues. Whereas for the cluster $[Os_3(CO)_{10}(bpym)]$ open-structure dianions are fairly stable in butyronitrile, no such products could be detected by IR spectroscopy for the corresponding triruthenium clusters.

Frontier orbitals and electronic transitions

A comparison of the frontier orbitals of $[Ru_3(CO)_8(\mu\text{-}CO)_2(bpy)]$ (**1″**) (Table 7) with those of $[Os_3(CO)_{10}(bpy)]$[57] reveals that the HOMOs of both clusters are clearly different with respect to the bonding interactions. While the HOMO of the triosmium cluster is mainly σ-bonding with regard to the (bpy)Os1–Os3 bond, the HOMO of $[Ru_3(CO)_8(\mu\text{-}CO)_2(bpy)]$ is best described as a π(Ru/μ-CO) bonding orbital and therefore antibonding with regard to the Ru1–Ru3 bond. Interestingly, the contribution of the π*(α-diimine) orbital to the LUMO is larger in **1″** (85%) than in the corresponding osmium cluster (76%), at the expense of its contribution to the HOMO (4% *vs.* 19%). On the other hand, the bridging carbonyl ligands, that are not present in $[Os_3(CO)_{10}(bpy)]$, contribute significantly to the HOMO of **1″** (36%) while their contribution to the LUMO is negligible (1%). Based on the compositions of the frontier orbitals, the HOMO–LUMO transition in $[Ru_3(CO)_8(\mu\text{-}CO)_2(bpy)]$ is best described as a π(Ru/μ-CO)⟶π*(α-diimine) charge-transfer transition.

In general, CT transitions possessing sigma-bond-to-L (SBLCT or σπ*),[58] metal-to-L (MLCT)[59–61] or halide-to-L (XLCT)[31,62] (L = α-diimine) charge-transfer character, are characterized by solvatochromism of the corresponding absorption band. However, negligible solvatochromism has been observed for the intense 471 nm band of cluster **1**. Moreover, the absorption maximum of this band is also not influenced by decreasing the energy of the lowest π* orbital of the α-diimine ligand on going from dmb to bpy and bpym. On the other hand, resonance Raman (rR) spectra of clusters **1** and **3** obtained by irradiation into this visible band show strong rR effects for Raman bands belonging to the vibronically coupled ν_s(CC) and ν_s(CN) stretching modes of the α-diimine and the ν_s(CO) mode, similar to the solvatochromic clusters $[Os_3(CO)_{10}(L)]$ (L = bpy, bpym).[20] Importantly, distinct rR effects are also observed for several bands in the region 600–220 cm^{-1}, belonging to metal–carbon stretching and M–C–O deformation modes.[28] The resonant enhancement of such skeletal modes points to the participation of the metal(carbonyl) core in the lowest allowed electronic transition that is directed towards the α-diimine ligand.

The assignment of the electronic transitions in the studied triruthenium α-diimine clusters has been obtained from time-dependent DFT calculations of cluster **1″** (Table 8). Their intense absorption band around 470 nm belongs predominantly to an allowed cluster core-to-ligand, σ(Ru_3)⟶π*(α-diimine), charge-transfer transition (transition 3 in Table 8), rather than to the HOMO–LUMO transition that has a very low oscillator strength. This assignment is in line with the experimental rR spectra: the appearance of Raman bands between 600 and 220 cm^{-1} indeed reveals the participation of the metal(carbonyl) core in this transition, while the resonantly enhanced intensities of the ν(CO) and internal α-diimine modes agree with a charge transfer to the α-diimine.

The absence of solvatochromism for the visible charge-transfer absorption band of $[Ru_3(CO)_8(\mu\text{-}CO)_2(\alpha\text{-diimine})]$ (**1**–**3**) in comparison with analogous but solvatochromic triosmium clusters[20] can arise from an interplay of several factors. First, the dipole moment change upon excitation may be smaller for the triruthenium clusters because of stronger σ-donation from the α-diimine (supported by apparent α-diimine dependence of the oxidation potentials of clusters **1**–**3**) and weaker Ru–α-diimine π-back-bonding. Second, the excitation predominantly originates in the HOMO−2 that is delocalized over the whole Ru_3 framework. Consequently, the charge change in clusters **1**–**3** is distributed over relatively large volume, demanding little solvent reorganisation. Third, the presence of the bridging carbonyls and the different orientation of the α-diimine ligand in clusters **1**–**3**, as compared with the triosmium clusters, may partly shield the parts of the molecule involved in excitation from the solvent molecules, diminishing the solvent response to excitation and, hence, the solvatochromism.

Apart from the negligible solvatochromism, changing the nature of the α-diimine ligand also does not affect the band maximum of the intense visible band. Replacing the α-diimine ligand by a better π-acceptor not only results in a stabilization of the π*(α-diimine) orbital but also lowers the energy of occupied frontier orbitals as a consequence of diminished (σ- and π-) donation from the α-diimine towards the cluster core. Although the redox potentials of the clusters **1**–**3** (Table 4) only prove the latter effect for their HOMO, this presumably also holds for the σ(Ru_3) HOMO−2. The energetic difference between the optical orbitals and, hence, also the σ(Ru_3)⟶π*(α-diimine) transition energy remain almost unaffected by the bpy and bpym variation.

In agreement with their low oscillator strengths, no well-resolved absorption bands due to the HOMO⟶LUMO and HOMO−1⟶LUMO transitions (transitions 1 and 2 in Table 8) are observed on the low-energy side of the 471 nm band. However, the weak absorption tailing to 650 nm is tentatively assigned to comprise the latter transitions. This assignment implies that the lowest-energy π(Ru/μ-CO)π*(α-diimine) excited state of the clusters $[Ru_3(CO)_8(\mu\text{-}CO)_2(\alpha\text{-diimine})]$ is optically hardly directly accessible.

At higher energy, a second group of fairly intense transitions is found, consisting of predominantly cluster core localized transitions directed to the LUMO+1 and LUMO+2 (transitions 8–10 in Table 8). As the absorption bands in the visible region are generally broad and poorly resolved, they likely consist of several close-lying transitions. In THF and MeCN a non-solvatochromic band is observed around 380 nm (see Fig. 2). As its position relative to the lowest-energy absorption band agrees reasonably well with the calculated energy difference between transitions 3 and 9 (Table 8), this band is tentatively attributed to one or more electronic transitions of the second group (transitions 8–10). In contrast, no such well-resolved absorption band is observed in this wavelength region for cluster **1** in toluene. Despite the fact that TD-DFT allows for mixing of the separate electronic transitions, the calculated excitation energies of the transitions in Table 8 are systematically lower by 0.6–0.7 eV than the experimental values. This difference is too large to be caused by the difference in medium between the theoretical and experimental data. Such discrepancies are, however, not uncommon for DFT calculations. They have been observed, for example, for transition metal complexes possessing metal–halide bonds.[63] Nevertheless, regardless of the relatively large differences, the calculated oscillator strengths compare reasonably well with the experimental band intensities in THF and MeCN and, in accordance with the rR spectra, predict the cluster core-to-ligand charge-transfer transition to dominate in the visible region.

Characterization of the excited states

In agreement with the rR spectra and the TD-DFT results, irradiation into the fairly intense 471 nm absorption band of the clusters $[Ru_3(CO)_8(\mu\text{-}CO)_2(\alpha\text{-diimine})]$ results in initial population of an excited state having predominant $\sigma(Ru_3)\pi^*(\alpha\text{-diimine})$ character, in which an electron has been transferred from a delocalized orbital that is bonding with regard to the cluster core to the lowest π^* orbital of the α-diimine ligand.

More insight into the decay kinetics and absorption features of the lowest excited state is obtained from the ps TA spectra. The initially observed transient absorption in the TA spectra of **1** and **3**, is ascribed to the lowest excited state of these clusters; it is very similar to the transient reported for the clusters $[Os_3(CO)_{10}(dmb)]$.[25] The close correspondence of the spectra with those reported for the latter clusters, together with the characteristic long-wavelength tail due to intraligand $\pi^*\pi^*$-(α-diimine) transitions, is in good agreement with the transfer of an electron to the lowest $\pi^*(\alpha\text{-diimine})$ orbital and the concomitant formation of α-diimine-localized radical anions. The ps TA spectra do not unambiguously reveal whether this electron originates from a molecular orbital with predominant π(Ru/μ-CO) character (HOMO) or delocalized $\sigma(Ru_3)$ (HOMO−2) character. The spectra observed for **1** and **3** at t_d = 1 ps are also very similar to the TA spectra observed for **2** in 2-MeTHF glass on the nanosecond time scale. This implies that the transient absorption band in the ns TA spectra of **2** can also be ascribed to the lowest excited state, its lifetime in a rigid matrix being extended into the nanosecond time domain. The excited-state lifetime of 43 ps, derived from the ps TA measurements of **2**, is significantly longer than the lifetime of 5 ps reported for $[Os_3(CO)_{10}(dmb)]$.[25] It is noteworthy that the ps TA spectra do not reveal the formation of open-structure biradicals from the excited state. The formation of these primary photoproducts is expected[25] to result in a characteristic, weak long-wavelength absorption without a distinct maximum that disappears upon regeneration of the parent cluster on the nanosecond time scale. Apparently, the formation of biradicals $[^{\bullet}Ru(CO)_4\text{–}Ru(CO)_4\text{–}^{+}Ru(CO)_2(dmb^{\bullet-})]$ from the excited state is less efficient than for the corresponding triosmium clusters, resulting in amounts not detectable by ps TA spectroscopy. This conclusion is in line with the increased excited-state lifetime and most likely has its origin in the presence of bridging carbonyl ligands in the clusters (*vide infra*).

The ps TRIR spectra provide a better understanding of the character of the lowest excited state. As described above, the excitation of cluster **2** results in the instantaneous appearance of a ν(μ-CO) band at 1778 cm^{-1}, *ca.* 35 cm^{-1} higher in frequency than found for the ground state. The shift of the ν(μ-CO) band to larger wavenumbers in the excited state is indicative of increased C–O bond order, resulting from depopulation of the π^*(μ-CO) orbitals. As the contribution of the π^*(μ-CO) orbitals to the HOMO−2 and LUMO is negligible (Table 7), population of the corresponding $\sigma(Ru_3)\pi^*(\alpha\text{-diimine})$ excited state cannot account for the observed large shift of the ν(μ-CO) band. On the other hand, the IR spectral changes are in good agreement with the lowest excited state having a predominant $\pi(Ru/\mu\text{-}CO)\pi^*(\alpha\text{-diimine})$ (HOMO/LUMO) character with major involvement of the π^*(μ-CO) orbitals (Table 7, Fig. 12). The ps TRIR spectral changes in the terminal ν(CO) region are also in favour of this assignment. According to the characters of the HOMO−2 and LUMO (Table 7), the population of the $\sigma(Ru_3)\pi^*(\alpha\text{-diimine})$ excited state reduces the electron density at the terminal carbonyls and should result in a shift of the corresponding ν(CO) bands to larger wavenumbers. In contrast to this, the TRIR spectra show a shift of the terminal ν(CO) bands in the opposite direction, indicating slightly increased Ru–to–CO π-back-donation. As the contribution of the terminal carbonyl ligands to the HOMO is relatively small, the slight decrease in π-back-bonding upon population of the $\pi(Ru/\mu\text{-}CO)\pi^*(\alpha\text{-diimine})$ excited state becomes compensated by the increased donation of the temporarily reduced α-diimine ligand. Based on the ps TRIR spectra, it is therefore concluded that the lowest excited state has a $\pi(Ru/\mu\text{-}CO)\pi^*(\alpha\text{-diimine})$ character. Both the UV–VIS spectra and TD-DFT results however show that this state is optically hardly directly accessible. Instead, the $\sigma(Ru_3)\pi^*(\alpha\text{-diimine})$ excited state is initially populated upon visible excitation. Population of the lowest $\pi\pi^*$ excited state is then proposed to take place *via* fast decay from the $\sigma(Ru_3)\pi^*(\alpha\text{-diimine})$ state on the sub-picosecond time scale. The assignment of the lowest excited state as $\pi(Ru/\mu\text{-}CO)\pi^*$-(α-diimine) also implies that the absorption features in the ps TA spectra of **1** and **3** belong to the same excited state. In line with this assignment, the excited-state lifetime of **2** of 45.5 ps, determined by Gaussian curve fitting on the ν(μ-CO) band at 1778 cm^{-1} (Fig. 4(b)), closely resembles the lifetime obtained from the TA experiments (43 ps). The close correspondence between the ps TA spectra of $[Ru_3(CO)_8(\mu\text{-}CO)_2(bpy)]$ and its triosmium analogue furthermore proves that the observed transient absorptions are hardly influenced by the nature of the initial optical orbital and can mainly be ascribed to the temporarily reduced α-diimine ligand.

Photochemical formation of open-structure products

The spectral changes observed in the ps TA and TRIR experiments are in good agreement with the $\pi(Ru/\mu\text{-}CO)\pi^*$-(α-diimine) character of the lowest excited state. As discussed above, this excited state is populated *via* fast decay from the initially populated $\sigma(Ru_3)\pi^*(\alpha\text{-diimine})$ excited state on the sub-picosecond time scale. In this respect, the studied $[Ru_3(CO)_8(\mu\text{-}CO)_2(\alpha\text{-diimine})]$ clusters differ significantly from the corresponding triosmium derivatives, for which the lowest $\sigma(Os1\text{–}Os3)\pi^*(\alpha\text{-diimine})$ excited state is directly optically accessible. Apart from this difference in population, the nature of the lowest excited state also has a marked influence on the formation of open-structure photoproducts. For the analogous triosmium clusters, population of the lowest $^3\sigma(Os1\text{–}Os3)\pi^*$-(α-diimine) excited state will result in a weakening of the Os1–Os3(α-diimine) bond.[57] In contrast, the depopulation of the HOMO of **1**–**3** will merely weaken the bonds between Ru1/Ru3 and the bridging carbonyls, but will not directly affect

the Ru1–Ru3 bond. The $[Ru_3(CO)_8(\mu\text{-}CO)_2(\alpha\text{-diimine})]$ clusters will therefore experience a higher energetic barrier for metal–metal bond cleavage and formation of open-structure photoproducts from the lowest excited state. As Ru–Ru(α-diimine) bond cleavage is the first step in the formation of open-structure photoproducts such as biradicals and zwitterions, the efficiency of their formation will be significantly lower for $[Ru_3(CO)_8(\mu\text{-}CO)_2(\alpha\text{-diimine})]$ than for the corresponding osmium clusters. This is indeed the case, since only a minor amount of biradicals was formed in the case of the $[Ru_3(CO)_8(\mu\text{-}CO)_2(\alpha\text{-diimine})]$ clusters, as was revealed by the detection of spin-trapped radicals with EPR and by the ps TRIR spectra of **2**. The reduced efficiency to form open-structure photoproducts is also reflected in the forcing experimental conditions required to obtain zwitterions. Whereas for the osmium clusters formation of zwitterions is already observed in coordinating solvents such as MeCN at room temperature or in THF at low temperatures (223 K), no photoproducts could be detected for the corresponding ruthenium clusters under similar conditions. Only in strongly coordinating media, such as in pyridine at 250 K, the formation of the photoproducts $\mathbf{1}_{zw}$**(py)**, $\mathbf{2}_{zw}$**(Br$^-$)** and $\mathbf{3}_{zw}$**(py)** was observed. Besides, the formation of zwitterions has a very low quantum yield. This is inferred from the long irradiation time and high laser power that are required to form zwitterions in detectable amounts.

It remains unravelled whether the zwitterions $\mathbf{1}_{zw}$**(py)**, $\mathbf{2}_{zw}$**(Br$^-$)** and $\mathbf{3}_{zw}$**(py)** are formed directly from the excited state or *via* the intermediate formation of the open-structure biradicals $[^{\bullet}Ru(CO)_4\text{–}Ru(CO)_4\text{–}^{+}Ru(Sv)(CO)_2(\alpha\text{-diimine}^{\bullet-})]$. For the corresponding triosmium clusters, both pathways operate, the latter one being more important.[25]

Summarizing, the influence of the bridging CO ligands on the observed photochemical reactivity is twofold. First of all, it makes the Ru1–Ru3 bond more difficult to break, which increases the energetic barrier for the formation of open-structure photoproducts. Second, the presence of bridging carbonyl ligands results in a different character of the HOMO that, in contrast to the analogous triosmium clusters, can be best described as a π(Ru/μ-CO) bonding and π*(Ru–Ru) antibonding orbital. As a result, population of the lowest ππ* (HOMO-to-LUMO) excited state hardly affects the Ru1–Ru3 bond. Both effects reduce the efficiency of the formation of biradicals and zwitterions and are reflected in the forcing experimental conditions required to obtain such products.

Conclusions

The presence of the bridging carbonyl ligands in $[Ru_3(CO)_8(\mu\text{-}CO)_2(\alpha\text{-diimine})]$ is found to have a marked influence on the photochemical reactivity of these clusters. Importantly, the character of the HOMO of the ruthenium clusters is different from that of the corresponding orbital of $[Os_3(CO)_{10}(\alpha\text{-diimine})]$ (α-diimine = bpy, bpym), the HOMO being best described as a π(Ru/μ-CO) bonding orbital. In contrast to the triosmium α-diimine clusters, the lowest π(Ru/μ-CO)π*(α-diimine) excited state is optically hardly directly accessible, the σ(Ru_3)π*(α-diimine) excited state being initially populated upon visible excitation. From the latter state fast decay to the lowest π(Ru/μ-CO)π*(α-diimine) excited state takes place on the sub-picosecond time scale. The specific character of this state and the presence of CO bridges prevent the efficient formation of open-structure photoproducts such as biradicals and zwitterions. In contrast to the corresponding triosmium clusters, the latter photoproduct was only obtained under forcing experimental conditions such as in strongly coordinating pyridine at 250 K.

The fairly high stability of the radical anions formed upon reduction of $[Ru_3(CO)_8(\mu\text{-}CO)_2(\alpha\text{-diimine})]$ clearly reflects the strong influence of the CO bridges also on the electrochemical reactivity. By contrast, the open-structure intermediates formed along the reduction path towards $[Ru(CO)_2(\alpha\text{-diimine})]_n$ and $[Ru_2(CO)_8]^{2-}$ are less stable than their triosmium analogues.

In general, the combination of the employed experimental photo- and electrochemical techniques together with the theoretical support from DFT and TD-DFT calculations has provided a realistic understanding of the bonding properties and reactivity of the intriguing $[Ru_3(CO)_8(\mu\text{-}CO)_2(\alpha\text{-diimine})]$ clusters, demonstrating the power of this approach in the field of transition metal cluster chemistry.

Experimental

Materials and preparations

Solvents of analytical grade (Acros: acetonitrile (MeCN), butyronitrile (PrCN), dichloromethane (CH_2Cl_2), diethyl ether (Et_2O), dimethoxyethane (DME), hexane, pentane, tetrahydrofuran (THF), toluene) or spectroscopic grade (Janssen: 2-MeTHF) were freshly distilled from sodium wire (Et_2O, DME, hexane, pentane, toluene, 2-MeTHF), sodium/benzophenone (THF) or CaH_2 (MeCN, PrCN, CH_2Cl_2) under an atmosphere of dry N_2. $[Ru_3(CO)_{12}]$ (Strem Chemicals), 2,2′-bipyridine (Merck), 4,4′-dimethyl-2,2′-bipyridine (Fluka), 2,2′-bipyrimidine (Alfa) and ferrocene (BDH) were used as received. Trimethylamine *N*-oxide, $Me_3NO{\cdot}2H_2O$ (Alfa), was dehydrated before use by vacuum sublimation. The supporting electrolyte Bu_4NPF_6 (Aldrich) was recrystallized twice from ethanol and dried *in vacuo* at 350 K overnight. Silica 60 (70–230 mesh, Merck) and neutral aluminium oxide 90 (70–230 mesh, Merck) for column chromatography were activated by heating *in vacuo* at 450 K overnight and stored under N_2. The reducing agent $[Fe^{I}(Cp)(C_6Me_6)]$ (Cp = η^5-C_5H_5) was prepared by reduction of $[Fe^{II}(Cp)(\eta^6\text{-}C_6Me_6)]PF_6$ with 1% Na/Hg in DME according to a literature procedure.[64]

Synthetic procedures

All syntheses were performed under an atmosphere of dry N_2, using standard Schlenk techniques.

Syntheses of $[Ru_3(CO)_8(\mu\text{-}CO)_2(bpy)]$ (1) and $[Ru_3(CO)_8(\mu\text{-}CO)_2(dmb)]$ (2). Cluster **1** was prepared according to a literature procedure[65] and purified by column chromatography (activated aluminium oxide, hexane/CH_2Cl_2 gradient elution). Cluster **2** was prepared by the same procedure and assigned by analogy with **1**. Both products were obtained as deep red powders in 70–80% yield.

$[Ru_3(CO)_8(\mu\text{-}CO)_2(bpy)]$. δ_H (300 MHz, $CDCl_3$) (for numbering scheme see Fig. 1) 9.95 (d, ^3J = 5 Hz, 2H, H_6), 8.29 (d, ^3J = 8.1 Hz, 2H, H_3), 8.07 (dd, ^3J = 8 Hz, ^3J = 7.5 Hz, 2H, H_4), 7.74 (dd, ^3J = 7.5 Hz, ^3J = 5 Hz, 2H, H_5). FAB$^+$ MS: *m*/*z* 740.74 $(M)^+$ (calculated 740.73), $(M)^+ - n$CO (n = 1–9).

$[Ru_3(CO)_8(\mu\text{-}CO)_2(dmb)]$. δ_H (300 MHz, $CDCl_3$) 9.73 (d, ^3J = 5.7 Hz, 2H, H_6), 8.07 (s, 2H, H_3), 7.51 (d, ^3J = 5.7 Hz, 2H, H_5), 2.63 (s, 6H, CH_3). FAB$^+$ MS: *m*/*z* 768.77 $(M)^+$ (calculated 768.76), $(M)^+ - n$CO (n = 1–7).

Synthesis of $[Ru_3(CO)_8(\mu\text{-}CO)_2(bpym)]$ (3). The synthesis of cluster **3** has already been reported by Cabeza *et al.*[66] who characterized it merely by microanalysis and IR spectroscopy (Nujol) owing to its reported high insolubility in common organic solvents. Here, however, we present a new synthetic procedure, resulting in a product that dissolves fairly well (in CH_2Cl_2, THF and MeCN) and could be characterized by ^{1}H NMR and IR spectroscopies and mass spectrometry.

A solution of Me_3NO (82.0 mg, 1.08 mmol) in 15 ml CH_2Cl_2 was added dropwise to a cooled (200 K) solution of $[Ru_3(CO)_{12}]$ (300 mg, 0.47 mmol) and bpym (96.4 mg, 0.61 mmol) in 150 ml

CH_2Cl_2. Next, the mixture was stirred for 2.5 h while warming up to room temperature. When almost all (>90%) $[Ru_3(CO)_{12}]$ was consumed, the solution was filtered over a short column of activated aluminium oxide. After evaporation of the solvent *in vacuo*, the product was purified by column chromatography (activated aluminium oxide, hexane/CH_2Cl_2 gradient elution). The product was obtained as a purple powder (105 mg, 30% yield). Depending on the dryness of Me_3NO, extra equivalents may be necessary to drive the reaction to completion. δ_H (300 MHz, $CDCl_3$) 10.14 (dd, ^3J = 5.7 Hz, ^4J = 2.4 Hz, 2H, H_6), 9.24 (dd, ^3J = 4.5 Hz, ^4J = 2.4 Hz, 2H, H_4), 7.85 (dd, ^3J = 5.4 Hz, ^3J = 4.8 Hz, 2H, H_5); FAB$^+$ MS: *m*/*z* 742.71 (M^+) (calculated 742.72), (M^+) − *n*CO (*n* = 1–9).

Syntheses of $[Ru(CO)_2(dmb)(I)_2]$ and $[\{Ru(CO)_2(I)_2\}_2$-(μ-bpym)]. $[Ru(CO)_2(dmb)(I)_2]$ was synthesized according to a literature procedure.[67] Applying this procedure for the synthesis of its bpym analogue resulted instead in the formation of the dinuclear complex $[\{Ru(CO)_2(I)_2\}_2(\mu\text{-bpym})]$ with a bridging bpym ligand.[68] $[\{Ru(CO)_2(I)_2\}_2(\mu\text{-bpym})]$ was prepared by suspending a mixture of $[Ru(CO)_2(I)_2(MeCN)_2]$ (1.055 g, 2.14 mmol) and bpym (375 mg, 2.37 mmol) in 50 ml Et_2O and heating it to reflux for 30 min. Next, the reaction mixture was cooled to room temperature. The residue was filtered off (G3 glass filter), washed with pentane and dried *in vacuo* to yield the product as a yellow powder (944 mg, 45% yield).

$[Ru(CO)_2(dmb)(I)_2]$. IR (THF): ν(CO)/cm^{-1} 2048vs, 1989vs; δ_H (300 MHz, CH_2Cl_2) 8.94 (d, ^3J = 5.8 Hz, 2H, H_6), 8.07 (s, 2H, H_3), 7.44 (d, ^3J = 5.5 Hz, 2H, H_5), 2.62 (s, 6H, CH_3).

$[\{Ru(CO)_2(I)_2\}_2(\mu\text{-bpym})]$. IR (THF): ν(CO)/cm^{-1} 2056vs, 2001vs; δ_H (300 MHz, CH_2Cl_2) 9.24 (d, ^3J = 15 Hz, 4H, $H_{4/6}$), 7.75 (t, ^3J = 4.8 Hz, 2H, H_5).

Spectroscopic measurements

FTIR spectra were obtained with Bio-Rad FTS-7 and Bio-Rad FTS-60A spectrometers (16 scans at 2 cm^{-1} resolution), the latter being equipped with a dual-source Digital Model 896 interferometer and a nitrogen-cooled MCT detector. The sample compartment of the Bio-Rad FTS-60A spectrometer was modified to allow *in situ* laser irradiation into a thermostated cell. Electronic absorption spectra were recorded on a Hewlett–Packard 8453 diode-array spectrophotometer, ^{1}H NMR spectra on a Bruker AMX 300 (300.13 MHz for ^{1}H) spectrometer and EPR spectra on a Varian Century E-104A spectrometer. EPR *g*-values were determined using 2,2′-diphenyl-1-picrylhydrazyl (DPPH, Aldrich) as an external standard (*g* = 2.0037). Linewidths and hyperfine splitting constants were derived from simulated spectra generated with PEST Winsim (version 0.96).[69] Mass spectra were collected on a JEOL JMS SX/SX102A four-sector mass spectrometer. Resonance Raman measurements were performed using a Dilor Modular XY spectrometer equipped with a Wright Instruments CCD detector. The solutions of the clusters in CH_2Cl_2 were placed in a spinning cell. The resonance Raman spectra were obtained at room temperature by excitation with the 457.9, 476.5, 488.0 and 514.5 nm lines of a Spectra Physics Model 2040E argon-ion laser.

Photochemistry

The 488.0 nm line of a Spectra Physics Model 2016 argon-ion laser was used for the continuous-wave irradiation experiments. All photochemical samples were prepared under a nitrogen atmosphere, using standard inert-gas techniques, and typically 10^{-3}–10^{-4} mol dm^{-3} cluster concentrations. Low-temperature IR and UV–VIS measurements were performed using an Oxford Instruments DN 1704/54 liquid nitrogen-cooled cryostat with CaF_2 and quartz windows.

Nanosecond transient absorption (ns TA) spectra were obtained by irradiating the samples with 2 ns pulses of the 470 nm line (typically 5 mJ pulse^{-1}) of a tunable (420–710 nm) Coherent Infinity XPO laser. The probe light from a low-pressure, high power EG&G FX-504 Xe lamp was passed through the sample cell and dispersed by an Acton Spectra-Pro-150 spectrograph equipped with 150 g mm^{-1} or 600 g mm^{-1} grating and a tuneable slit (1–500 μm), resulting in a 6 or 1.2 nm maximum resolution, respectively. The data collection system consisted of a gated intensified CCD detector (Princeton Instruments ICCD-576EMG/RB), a programmable pulse generator (PG-200), and an EG&G Princeton Applied Research Model 9650 digital delay generator. Picosecond transient absorption (ps TA) spectra were recorded using the set-up installed at the University of Amsterdam.[25] Part of the 800 nm output of a Ti:sapphire regenerative amplifier (1 kHz, 130 fs, 1 mJ) was focussed into a H_2O flow-through cell (10 mm; Hellma) to generate white light. The residual part of the 800 nm fundamental was used to provide 505 nm (fourth harmonic of the 2020 OPA idler beam) excitation pulses with a general output of 5 μJ pulse^{-1}. After passing through the sample, the probe beam was coupled into a 400 μm optical fibre and detected by a CCD spectrometer (Ocean Optics, PC2000). The chopper (Rofin Ltd., *f* = 10–20 Hz), placed in the excitation beam, provided *I* and I_0, depending on the status of the chopper (open or closed). The excited state spectra were obtained by $\Delta A = \log(I/I_0)$. Typically two thousand excitation pulses were averaged to obtain the transient at a particular time delay.

Picosecond time-resolved infrared (ps TRIR) spectra were recorded using the Picosecond Infrared Absorption and Transient Excitation (PIRATE) facility at the Rutherford Appleton Laboratory.[70] The laser system is based on a Ti:sapphire regenerative amplifier (Spectra Physics/Positive Light, Superspitfire), operating at 1 kHz repetition rate at *ca*. 800 nm, with an energy of 2–3 mJ pulse^{-1} (150 fs FWHM). Tuneable mid-IR outputs (150–200 cm^{-1} FWHM, 200 fs) were generated by frequency-down conversion of the signal and idler outputs of a white-light seeded, 800 nm pumped BBO OPA in an $AgGaS_2$ crystal. Second harmonic generation of the residual fundamental light (800 nm) provided 400 nm pulses, which were used to pump a second OPA, generating 500 nm excitation pulses. The mid-IR beam generated by the first OPA was split into reference and probe beams, using a 50% germanium beamsplitter. Below 1800 cm^{-1}, N_2-purged infrared beam paths were applied to reduce probe beam absorption by water vapour. The flow-through cell, consisting of two CaF_2 windows separated by 0.25–1 mm spacers, was allowed to make a rastering movement perpendicular to the probe beam in order to avoid local heating and sample decomposition by the laser beams. Two separate 64-element HgCdTe linear array detectors (MCT-13-64el (Infrared Associates Inc.) and MCT-64000 pre-amplifiers (Infrared Systems Development Corp.)) were used to detect the mid-IR reference and probe signals. TRIR spectra comprising the whole CO-stretching region (2200–1700 cm^{-1}) were constructed by precise overlap of three or four 150 cm^{-1} windows. Calibration of the spectra was established by comparing the parent bleach positions with the peak positions of the corresponding ν(CO) bands in the regular FTIR spectra.

Electrochemistry

Cyclic voltammograms (CV) of approximately 10^{-3} M parent clusters in 10^{-1} M Bu_4NPF_6 electrolyte solution were recorded in a gas-tight, single-compartment, three-electrode cell equipped with platinum disc working (apparent surface of 0.42 mm^2), coiled platinum wire auxillary and silver wire pseudo-reference electrodes. The cell was connected to a computer-controlled PAR Model 283 potentiostat. All redox potentials are reported against the ferrocene–ferrocenium (Fc/Fc^+) redox couple.[71,72] IR and UV–VIS spectroelectrochemical

measurements were performed with previously described optically transparent thin-layer electrochemical (OTTLE) cells[73,74] equipped with a Pt minigrid working electrode (32 wires/cm) and CaF_2/NaCl or CaF_2/quartz windows. The working electrode surroundings were masked carefully to avoid spectral interference with the non-electrolyzed solution. EPR spectra of the electrogenerated radicals were recorded at variable temperatures, using a modified three-electrode Allendoerfer-type[75] spectroelectrochemical cell equipped with a single-point Ag pseudo-reference electrode. The potential during these measurements was controlled by a PA4 (EKOM, Czech Republic) potentiostat. The cluster concentration in the spectroelectrochemical experiments varied from 10^{-3} (UV–VIS, EPR) to 5×10^{-3} (IR) mol dm^{-3}.

Computational details

All density functional theoretical (DFT) calculations[76] were carried out with the Amsterdam Density Functional (ADF2000) programme.[77–83] Vosko, Wilk and Nusair's local exchange correlation potential was used.[84] Gradient-corrected geometry optimizations[85,86] were performed, using the Generalized Gradient Approximation (Becke's exchange[87] and Perdew's correlation[88,89] functionals). Relativistic effects were treated by the ZORA method.[90–92] The core orbitals were frozen for Ru (1s–4s, 1p–4p, 3d) and C, N, O (1s). Triple ζ Slater-type orbitals (STO) were used to describe the valence shells of H (1s), C and O (2s and 2p) and Ru (4d, 5s and 5p). A set of polarization functions was added: H (single ζ, 2p, 3d), C, N, O (single ζ, 3d, 4f), Ru (single ζ, 4f). Full geometry optimizations were performed without any symmetry constraints on clusters based on the available crystal structure of cluster **1**.[45,65]

Acknowledgements

Professors D. J. Stufkens (Universiteit van Amsterdam) and A. Vlček Jr. (Queen Mary and Westfield College, University of London) are gratefully acknowledged for their interest in this work and stimulating scientific discussions. We thank Mr. T. Mahabiersing (Universiteit van Amsterdam) for having performed the spectro-electrochemical experiments with the reference complexes $[Ru(CO)_2(dmb)(I)_2]$ and $[\{Ru(CO)_2(I)_2\}_2(\mu\text{-bpym})]$, and Mr. P. J. Costa (ITQB, Oeiras) for the DFT calculations on isomer **1‴**. This work has been undertaken as a part of the European collaborative COST project (D14/0001/99). Financial support has been received from the Council for Chemical Sciences of the Netherlands Organization for Scientific Research (CW-NWO, project No. 348–032; F.W.V. and F.H.) and from the European Union (LSF ref. No. USEV13C2/01).

References

1 M. G. Richmond, *Coord. Chem. Rev.*, 1997, **160**, 237.
2 A. Darchen, C. Mahé and H. Patin, *J. Chem. Soc., Chem. Commun.*, 1982, 243.
3 N. E. Leadbeater, *J. Organomet. Chem.*, 1999, **573**, 211.
4 N. E. Leadbeater, *J. Chem. Soc., Dalton Trans.*, 1995, 2923.
5 D. R. Tyler, M. Altobelli and H. B. Gray, *J. Am. Chem. Soc.*, 1980, **102**, 3022.
6 J. Malito, S. Markiewicz and A. Poë, *Inorg. Chem.*, 1982, **21**, 4335.
7 A. J. Poë and C. V. Sekhar, *J. Am. Chem. Soc.*, 1986, **108**, 3673.
8 F.-W. Grevels, W. E. Klotzbücher, J. Schrickel and K. Schaffner, *J. Am. Chem. Soc.*, 1994, **116**, 6229.
9 P. C. Ford, *J. Organomet. Chem.*, 1990, **383**, 339.
10 J. A. Dibenedetto, D. W. Ryba and P. C. Ford, *Inorg. Chem.*, 1989, **28**, 3503.
11 M. F. Desrosiers, D. A. Wink, R. Trautman, A. E. Friedman and P. C. Ford, *J. Am. Chem. Soc.*, 1986, **108**, 1917.
12 M. F. Desrosiers and P. C. Ford, *Organometallics*, 1982, **1**, 1715.
13 J. G. Bentsen and M. S. Wrighton, *J. Am. Chem. Soc.*, 1987, **109**, 4518.
14 J. G. Bentsen and M. S. Wrighton, *J. Am. Chem. Soc.*, 1987, **109**, 4530.
15 F. W. Vergeer, F. Hartl, P. Matousek, D. J. Stufkens and M. Towrie, *Chem. Commun.*, 2002, 1220.
16 M. J. Bakker, F. Hartl, D. J. Stufkens, O. S. Jina, X.-Z. Sun and M. W. George, *Organometallics*, 2000, **19**, 4310.
17 J. Nijhoff, M. J. Bakker, F. Hartl, D. J. Stufkens, W.-F. Fu and R. van Eldik, *Inorg. Chem.*, 1998, **37**, 661.
18 J. Nijhoff, F. Hartl, J. W. M. van Outersterp, D. J. Stufkens, M. J. Calhorda and L. F. Veiros, *J. Organomet. Chem.*, 1999, **573**, 121.
19 J. Nijhoff, F. Hartl, D. J. Stufkens and J. Fraanje, *Organometallics*, 1999, **18**, 4380.
20 J. W. M. van Outersterp, M. T. Garriga Oostenbrink, H. A. Nieuwenhuis, D. J. Stufkens and F. Hartl, *Inorg. Chem.*, 1995, **34**, 6312.
21 M. J. Bakker, F. W. Vergeer, F. Hartl, O. S. Jina, X.-Z. Sun and M. W. George, *Inorg. Chim. Acta*, 2000, **300–302**, 597.
22 M. J. Bakker, F. W. Vergeer, F. Hartl, P. Rosa, L. Ricard, P. Le Floch and M. J. Calhorda, *Chem. Eur. J.*, 2002, **8**, 1741.
23 F. W. Vergeer, M. J. Calhorda, F. Hartl, M. Lutz and A. L. Spek, unpublished work.
24 S. Chardon-Noblat and A. Deronzier, personal communication.
25 F. W. Vergeer, C. J. Kleverlaan and D. J. Stufkens, *Inorg. Chim. Acta*, 2002, **327**, 126.
26 S. McClanahan and J. Kincaid, *J. Raman Spectrosc.*, 1984, **15**, 173.
27 W. Kaim, S. Kohlmann, A. J. Lees, T. L. Snoeck, D. J. Stufkens and M. M. Zulu, *Inorg. Chim. Acta*, 1993, **210**, 159.
28 S. F. A. Kettle and P. L. Stanghellini, *Inorg. Chem.*, 1979, **18**, 2749.
29 M. P. Aarnts, D. J. Stufkens, M. P. Wilms, E. J. Baerends, A. Vlček Jr., I. P. Clark, M. W. George and J. J. Turner, *Chem. Eur. J.*, 1996, **2**, 1556.
30 B. D. Rossenaar, E. Lindsay, D. J. Stufkens and A. Vlček Jr., *Inorg. Chim. Acta*, 1996, **250**, 5.
31 B. D. Rossenaar, D. J. Stufkens and A. Vlček Jr., *Inorg. Chem.*, 1996, **35**, 2902.
32 B. D. Rossenaar, D. J. Stufkens and A. Vlček Jr., *Inorg. Chim. Acta*, 1996, **247**, 247.
33 A. Klein and W. Kaim, *Organometallics*, 1995, **14**, 1176.
34 H. Yang, T. Snee, K. T. Kotz, C. K. Payne and C. B. Harris, *J. Am. Chem. Soc.*, 2001, **123**, 4204.
35 J. C. Owrutsky and A. P. Baronavski, *J. Chem. Phys.*, 1996, **105**, 9864.
36 T. P. Dougherty and E. J. Heilweil, *Chem. Phys. Lett.*, 1994, **227**, 19.
37 T. P. Dougherty and E. J. Heilweil, *J. Chem. Phys.*, 1994, **100**, 4006.
38 F. Hartl and J. W. M. van Outersterp, unpublished work.
39 J. W. M. van Outersterp, Ph. D. Thesis, University of Amsterdam, 1995.
40 N. K. Bhattacharyya, T. J. Coffy, W. Quintana, T. A. Salupo, J. C. Bricker, T. B. Shay, M. Payne and S. G. Shore, *Organometallics*, 1990, **9**, 2368.
41 S. Chardon-Noblat, A. Deronzier, R. Ziessel and D. Zsoldos, *J. Electroanal. Chem.*, 1998, **444**, 253.
42 S. Chardon-Noblat, A. Deronzier, D. Zsoldos, R. Ziessel, M. Haukka, T. Pakkanen and T. Venäläinen, *J. Chem. Soc., Dalton Trans.*, 1996, 2581.
43 M.-N. Collomb-Dunand-Sauthier, A. Deronzier and R. Ziessel, *J. Chem. Soc., Chem. Commun.*, 1994, 189.
44 P. Homanen, M. Haukka, M. Ahlgren, T. A. Pakkanen, P. N. W. Baxter, R. E. Benfield and J. A. Connor, *J. Organomet. Chem.*, 1998, **552**, 205.
45 M. I. Bruce, M. G. Humphrey, M. R. Snow, E. R. Tiekink and R. C. Wallis, *J. Organomet. Chem.*, 1986, **314**, 311.
46 S. Portmann and H. P. Lüthi, *Chimia*, 2000, **54**, 766.
47 N. E. Leadbeater, J. Lewis, P. R. Raithby and G. N. Ward, *J. Chem. Soc., Dalton Trans.*, 1997, 2511.
48 M. R. Churchill and B. G. de Boer, *Inorg. Chem.*, 1977, **16**, 878.
49 M. R. Churchill, F. J. Hollander and J. P. Hutchinson, *Inorg. Chem.*, 1977, **16**, 2655.
50 B. D. Rossenaar, F. Hartl, D. J. Stufkens, C. Amatore, E. Maisonhaute and J.-N. Verpeaux, *Organometallics*, 1997, **16**, 4675.
51 D. Osella and J. Hanzlík, *Inorg. Chim. Acta*, 1993, **213**, 311.
52 A. J. Downard, B. H. Robinson and J. Simpson, *J. Organomet. Chem.*, 1987, **320**, 363.
53 C. Caix-Cecillon, S. Chardon-Noblat, A. Deronzier, M. Haukka, T. Pakkanen, R. Ziessel and D. Zsoldos, *J. Electroanal. Chem.*, 1999, **466**, 187.
54 M.-N. Collomb-Dunand-Sauthier, A. Deronzier and R. Ziessel, *Inorg. Chem.*, 1994, **33**, 2961.
55 A. Klein, C. Vogler and W. Kaim, *Organometallics*, 1996, **15**, 236.
56 J. W. M. van Outersterp, F. Hartl and D. J. Stufkens, *Organometallics*, 1995, **14**, 3303.

57 M. J. Calhorda, E. Hunstock, L. F. Veiros and F. Hartl, *Eur. J. Inorg. Chem.*, 2001, 223.
58 D. J. Stufkens, M. P. Aarnts, J. Nijhoff, B. D. Rossenaar and A. Vlček Jr., *Coord. Chem. Rev.*, 1998, **171**, 93.
59 D. J. Stufkens, *Comments Inorg. Chem.*, 1992, **13**, 359.
60 D. J. Stufkens, *Coord. Chem. Rev.*, 1990, **104**, 39.
61 A. J. Lees, *Coord. Chem. Rev.*, 1998, **177**, 3.
62 H. A. Nieuwenhuis, D. J. Stufkens and A. Oskam, *Inorg. Chem.*, 1994, **33**, 3212.
63 M. Turki, C. Daniel, S. Záliš, A. Vlček Jr., J. van Slageren and D. J. Stufkens, *J. Am. Chem. Soc.*, 2001, **123**, 11431.
64 D. Astruc, M. Hamon, M. Lacoste, M.-H. Desbois and E. Roman, in *Organometallic Synthesis*, ed. R. B. King, Amsterdam, 1988.
65 T. Venäläinen, J. Pursiainen and T. A. Pakkanen, *J. Chem. Soc., Chem. Commun.*, 1985, 1348.
66 J. A. Cabeza, L. A. Oro, A. Tiripicchio and M. Tiripicchio-Camellini, *J. Chem. Soc., Dalton Trans.*, 1988, 1437.
67 J. van Slageren and D. J. Stufkens, *Inorg. Chem.*, 2001, **40**, 277.
68 N. C. Thomas and J. Cox, *Polyhedron*, 1988, **7**, 731.
69 D. Duling, Public EPR Software Tools, National Institute of Environmental Health Sciences; http://epr.niehs.nih.gov/pest.html.
70 M. Towrie, D. C. Grills, J. Dyer, J. A. Weinstein, P. Matousek, R. Barton, P. D. Bailey, N. Subramaniam, W. M. Kwok, C. Ma, D. Phillips, A. W. Parker and M. W. George, *Appl. Spectrosc.*, 2003, **57**, 367.
71 G. Gritzner and J. Kůta, *Pure Appl. Chem.*, 1984, **56**, 461.
72 V. V. Pavlishchuk and A. W. Addison, *Inorg. Chim. Acta*, 2000, **298**, 97.
73 M. Krejčík, M. Daněk and F. Hartl, *J. Electroanal. Chem., Interfacial Electrochem.*, 1991, **317**, 179.
74 F. Hartl, H. Luyten, H. A. Nieuwenhuis and G. C. Schoemaker, *Appl. Spectrosc.*, 1994, **48**, 1522.
75 R. D. Allendoerfer, G. A. Martinchek and S. Bruckenstein, *Anal. Chem.*, 1975, **47**, 890.
76 R. G. Parr and W. Yang, in *Density Functional Theory of Atoms and Molecules*, New York, 1989.
77 E. J. Baerends, A. Bérces, C. Bo, P. M. Boerrigter, L. Cavallo, L. Deng, R. M. Dickson, D. E. Ellis, L. Fan, T. H. Fischer, C. Fonseca Guerra, S. J. A. van Gisbergen, J. A. Groeneveld, O. V. Gritsenko, F. E. Harris, P. van den Hoek, H. Jacobsen, G. van Kessel, F. Kootstra, E. van Lenthe, V. P. Osinga, P. H. T. Philipsen, D. Post, C. C. Pye, W. Ravenek, P. Ros, P. R. T. Schipper, G. Schreckenbach, J. G. Snijders, M. Sola, D. Swerhone, G. te Velde, P. Vernooijs, L. Versluis, O. Visser, E. van Wezenbeek, G. Wiesenekker, S. K. Wolff, T. K. Woo and T. Ziegler, *ADF 2000*.
78 C. Fonseca Guerra, O. Visser, J. G. Snijders, G. te Velde and E. J. Baerends, in *Parallelisation of the Amsterdam Density Functional Programme*, ed. E. Clementi and C. Corongiu, Cagliari, 1995.
79 C. Fonseca Guerra, J. G. Snijders, G. te Velde and E. J. Baerends, *Theor. Chem. Acc.*, 1998, **99**, 391.
80 E. J. Baerends, D. Ellis and P. Ros, *Chem. Phys.*, 1973, **2**, 41.
81 E. J. Baerends and P. Ros, *Int. J. Quantum Chem.*, 1978, **S12**, 169.
82 P. M. Boerrigter, G. te Velde and E. J. Baerends, *Int. J. Quantum Chem.*, 1988, **33**, 87.
83 G. te Velde and E. J. Baerends, *J. Comput. Phys.*, 1992, **99**, 84.
84 S. H. Vosko, L. Wilk and M. Nusair, *Can. J. Phys.*, 1980, **58**, 1200.
85 L. Versluis and T. Ziegler, *J. Chem. Phys.*, 1988, **88**, 322.
86 L. Fan and T. Ziegler, *J. Chem. Phys.*, 1991, **95**, 7401.
87 A. D. Becke, *J. Chem. Phys.*, 1987, **88**, 1053.
88 J. P. Perdew, *Phys. Rev. B*, 1986, **33**, 8822.
89 J. P. Perdew, *Phys. Rev. B*, 1986, **34**, 7406 (erratum).
90 A. Rosa, S. J. A. van Gisbergen, E. van Lenthe, J. A. Groeneveld and J. G. Snijders, *J. Am. Chem. Soc.*, 1999, **121**, 10356.
91 S. J. A. van Gisbergen, J. A. Groeneveld, A. Rosa, J. G. Snijders and E. J. Baerends, *J. Phys. Chem. A*, 1999, **103**, 6835.
92 S. J. A. van Gisbergen, A. Rosa, G. Ricciardi and E. J. Baerends, *J. Chem. Phys.*, 1999, **111**, 2499.